Thermal history of the central Gotthard and Aar massifs, European Alps: Evidence for steady state, long-term exhumation

C. Glotzbach, J. Reinecker, M. Danišík, M. Rahn, W. Frisch, C. Spiegel

Thermal history of the central Gotthard and Aar massifs, European Alps: Evidence for steady state, long-term exhumation

C. Glotzbach,[1,2] J. Reinecker,[3] M. Danišík,[4] M. Rahn,[5] W. Frisch,[3] and C. Spiegel[6]

Received 7 March 2009; revised 25 January 2010; accepted 23 February 2010; published 5 August 2010.

[1] Quantifying long-term exhumation rates is a prerequisite for understanding the geodynamic evolution of orogens and their exogenic and endogenic driving forces. Here we reconstruct the exhumation history of the central Aar and Gotthard external crystalline massifs in the European Alps using apatite and zircon fission track and apatite (U-Th)/He data. Age-elevation relationships and time-temperature paths derived from thermal history modeling are interpreted to reflect nearly constant exhumation of ~0.5 km/Ma since ~14 Ma. A slightly accelerated rate (~0.7 km/Ma) occurred from 16 to 14 Ma and again from 10 to 7 Ma. Faster exhumation between 16 and 14 Ma is most likely linked to indentation of the Adriatic wedge and related thrusting along the Alpine sole thrust, which, in turn, caused uplift and exhumation in the external crystalline massifs. The data suggest nearly steady, moderate exhumation rates since ~14 Ma, regardless of major exogenic and endogenic forces such as a change to wetter climate conditions around 5 Ma or orogen-perpendicular extension initiated in Pliocene times. Recent uplift and denudation rates, interpreted to be the result of climate fluctuations and associated increase in erosional efficiency, are nearly twice this ~0.5 km/Ma paleoexhumation rate.

Citation: Glotzbach, C., J. Reinecker, M. Danišík, M. Rahn, W. Frisch, and C. Spiegel (2010), Thermal history of the central Gotthard and Aar massifs, European Alps: Evidence for steady state, long-term exhumation, *J. Geophys. Res.*, *115*, F03017, doi:10.1029/2009JF001304.

1. Introduction

[2] The theoretical understanding of the relationship between tectonics, climate and erosion in driving the evolution of active mountain ranges has progressed recently [e.g., *Beaumont et al.*, 1992; *Willett et al.*, 1993; *Whipple and Meade*, 2006]. While field evidence to support the modeling is still sparse [e.g., *Whipple*, 2009, and references therein], studies of the European Alps, and especially the central Alps [e.g., *Kuhlemann*, 2007; *Schlunegger et al.*, 2007; *Willett et al.*, 2006; *Wittmann et al.*, 2007], reveal that climatic and tectonic processes have affected erosion and exhumation on different spatial and temporal scales.

[3] At the orogen-wide scale, sediment budget data and a compilation of thermochronological data independently suggest an increase of both the sediment flux out of the orogen and exhumation rates at ~5 Ma [*Kuhlemann*, 2000; *Willett et al.*, 2006; *Vernon et al.*, 2008]. On the regional scale, however, the increase in exhumation rate is not evident or occurred at a different time [*Bogdanoff et al.*, 2000; *Glotzbach et al.*, 2008; *Hurford*, 1986; *Wagner et al.*, 1977]. A thermochronological study on Molasse sediments of the North Alpine Foreland Basin found evidence of a rapid exhumation event at ~5 Ma [*Cederbom et al.*, 2004], and suggested this was a consequence of isostatic rebound caused by climate-triggered accelerated erosion of the Alps. *Willett et al.* [2006] interpreted the rapid exhumation of the Molasse sediments, together with the cessation of deformation in the Jura Mountains [*Becker*, 2000], as a backstepping of the deformation into the orogenic interior (external crystalline massifs) and evoked intensified erosion in response to wetter conditions as the causal event. In contrast, thermochronological studies in the direct hinterland of the North Alpine Foreland Basin, in the central Aar and Gotthard external crystalline massifs (AM and GM, respectively), found no increase in exhumation rates at ~5 Ma. Early studies suggested a long-lived exhumational steady state with rates of ~0.5 km/Ma [*Hurford*, 1986; *Schaer et al.*, 1975; *Wagner et al.*, 1977], and recent numerical thermal modeling of thermochronological data suggested that maybe exhumation was episodic, with faster exhumation from 9 to 7 Ma and 5 to 3 Ma (increasing from 0.3 to 0.7 km/Ma) [*Vernon et al.*, 2009].

[4] On a much shorter time scale, recent rock uplift rates derived from precise leveling reached ~1 mm/yr in the central Alps [*Kahle et al.*, 1997] and seemed to be balanced by similar denudation rates measured with in situ produced

[1]Laboratoire de Géodynamique des Chaînes Alpines, Observatoire des Sciences de l'Univers de Grenoble, Université Joseph Fourier, Grenoble, France.
[2]Now at Institute of Geology, University of Hannover, Hannover, Germany.
[3]Institute for Geoscience, University of Tübingen, Tübingen, Germany.
[4]John de Laeter Centre of Mass Spectrometry, Applied Geology, Curtin University of Technology, Perth, Western Australia, Australia.
[5]Institute of Geoscience, University of Freiburg, Freiburg, Germany.
[6]FB 5: Geoscience, University of Bremen, Bremen, Germany.

0148-0227/10/2009JF001304

cosmogenic ^{10}Be in quartz samples from central Alpine catchments averaging over the last 0.4–1.5 ka [*Wittmann et al.*, 2007]. Rapid denudation and rock uplift are probably the result of glacial erosion-induced rebound [*Barletta et al.*, 2006; *Champagnac et al.*, 2007, 2009]. *Champagnac et al.* [2007] suggested that about 50% of the observed vertical motion of the Western Alps is related to isostatic rebound due to enhanced Quaternary erosion rates.

[5] Beside this evidence for the coupling of climate forces and erosion/exhumation, a temporal coherence between accelerated exhumation and tectonic movement is suggested for parts of the central Alps. Thermal modeling of thermochronological data in the southwestern AM suggested an almost twofold increase in exhumation rates at ~3.5 Ma, [*Reinecker et al.*, 2008]. This acceleration in exhumation was synchronous with rotation of extension from orogen-parallel to orogen-perpendicular [e.g., *Sue et al.*, 2007] which initiated tectonic denudation in the footwall of the Rhône-Simplon fault. On the northeastern end of the AM, young thermochronological ages, postglacial faulting, elevated recent uplift rates and seismicity are interpreted to be the result of ongoing compression in the Alps [*Persaud and Pfiffner*, 2004]. GPS measurements of crustal deformation in central Europe, however, show that the central Alps and Western Alps are currently characterized by strike-slip and extensional movements, and compression is only found in the Eastern Alps [*Calais et al.*, 2002; *Nocquet and Calais*, 2004; *Sue et al.*, 2007].

[6] Complementary to the intensively studied Lötschberg transect in the southwestern AM [*Reinecker et al.*, 2008], the aim of this study is to gain detailed thermochronological constraints on the Neogene exhumation history of the central AM and GM. We apply zircon and apatite fission track, and apatite (U-Th)/He thermochronology along the Gotthard road tunnel and the corresponding surface line which intersects both massifs (in the following referred to as "Gotthard transect"). Our sampling strategy allowed the determination of horizontal and vertical age trends across the southeastern AM and GM, and the derivation of long-term cooling and exhumation rates. Results are compared to studies of surrounding regions [e.g., *Reinecker et al.*, 2008; *Vernon et al.*, 2008, 2009] which suggest different pulses of exhumation. Furthermore, the thermochronological data set is examined for evidence of climate change impacts and tectonic forces which may have controlled the exhumation pattern of the study area and of the central Alps.

2. Geological Setting

[7] The central Alps formed in response to convergent movements between Africa and Europe, resulting in the southward subduction of the Penninic Ocean and eventual continent-continent collision during the Tertiary [e.g., *Frisch*, 1979]. During this orogeny the European continental margin (Helvetic domain) was overthrust by the African continental margin (Austroalpine domain). Continental and oceanic crust fragments of the Penninic domain were squeezed in between [*Steck and Hunziker*, 1994]. Helvetic, Penninic and Austroalpine units were thrust northward, resulting in the burial of the now exposed external crystalline massifs (ECM). The ECMs (Aar, Gotthard, Tavetsch, Mont Blanc, Aiguilles Rouges, Belledone, Pelvoux, Argentera) are exposed orogen-parallel along the footwall of the Penninic frontal thrust [e.g., *Schmid et al.*, 2004]. They consist of pre-Variscan poly metamorphic basement (e.g., Caledonian rocks with ages of ~440–470 Ma) intruded by late Variscan granitoids (~290–340 Ma) and are covered by Palaeozoic to lower Tertiary sediments [*Labhart*, 1977; *Schaltegger*, 1994; *von Raumer and Neubauer*, 1993]. Peak Alpine metamorphic conditions were reached diachronously between ~35 and ~15 Ma [*Frey and Ferreiro Mählmann*, 1999]. The main uplift, exhumation and doming of the ECM and bending of the Helvetic basal thrust postdate the emplacement of the overlying Helvetic nappes [e.g., *Schmid et al.*, 2004], which took place between 32 and 15 Ma [e.g., *Kirschner et al.*, 1996]. The late stage of nappe emplacement (~20 Ma), however, led to thrusting and related exhumation in the ECM, as evidenced in the Mont Blanc and Tavetsch massifs [*Rolland et al.*, 2008; *Wyder and Mullis*, 1998]. After emplacement of the Helvetic nappes, thrusting propagated to the foreland along a crustal-scale ramp structure (Alpine sole thrust), which is kinematically linked to the Adriatic lower crustal wedge (Figure 1) [e.g., *Schmid et al.*, 1996]. The Alpine sole thrust is situated beneath the ECM, merges into the Jura basal décollement, and terminates in the Jura thrusts. Thrusting resulted in an imbrication of the crystalline basement, causing doming and steepening of structures in the ECM and overthrusting of the autochthonous Mesozoic cover [*Pfiffner et al.*, 1997a; *Schmid et al.*, 1996; *Wyder and Mullis*, 1998]. Much of the shortening of the basement was accommodated within the overlying Subalpine Molasse zone, and only a small fraction was transferred to movements along the Jura basal décollement. Related thrusting in the Jura Mountains [*Pfiffner et al.*, 1997a, 1997b] occurred between ~9 and ~4 Ma [*Becker*, 2000].

[8] In this study we investigate a transect intersecting the GM and the southern part of the AM (Figure 1). The boundary between the GM and AM is marked by Permo-Carboniferous and Mesozoic sediments of the heavily tectonized Urseren-Gavera Zone. To the east the Tavetsch massif crops out within the Urseren-Gavera Zone (Figure 1). The AM and the majority of the GM experienced greenschist facies metamorphism, whereas rocks exposed in the southern part of the GM reached amphibolite grade [*Frey and Ferreiro Mählmann*, 1999; *Frey et al.*, 1976]. Present-day rock uplift rates, determined by precise leveling [*Gubler*, 1976; *Kahle et al.*, 1997], increase to the south, with rates of ~1 mm/yr in the central Lepontine Dome, and maximum rates of ~1.5 mm/yr in two isolated areas around Brig and Chur (Figure 1). The study area is situated in between these maxima, and is characterized by recent rock uplift rates between 0.8 and 1.0 mm/yr.

3. Available Thermochronological Constraints

[9] Published zircon fission track (ZFT) ages of the AM range from 12 Ma in the southeast to ~100 Ma in the northwest (Figure 2) [*Michalski and Soom*, 1990; *Soom*, 1989], indicating that the ZFT system was only partially reset during Alpine metamorphism at the northwestern margin of the massif. ZFT ages from the Lepontine Dome, southeast of the GM, cluster between 11 and 14 Ma [*Dörr*, 2007; *Hurford*, 1986; *Steiner*, 1984]. ZFT ages from the GM itself have not been previously reported.

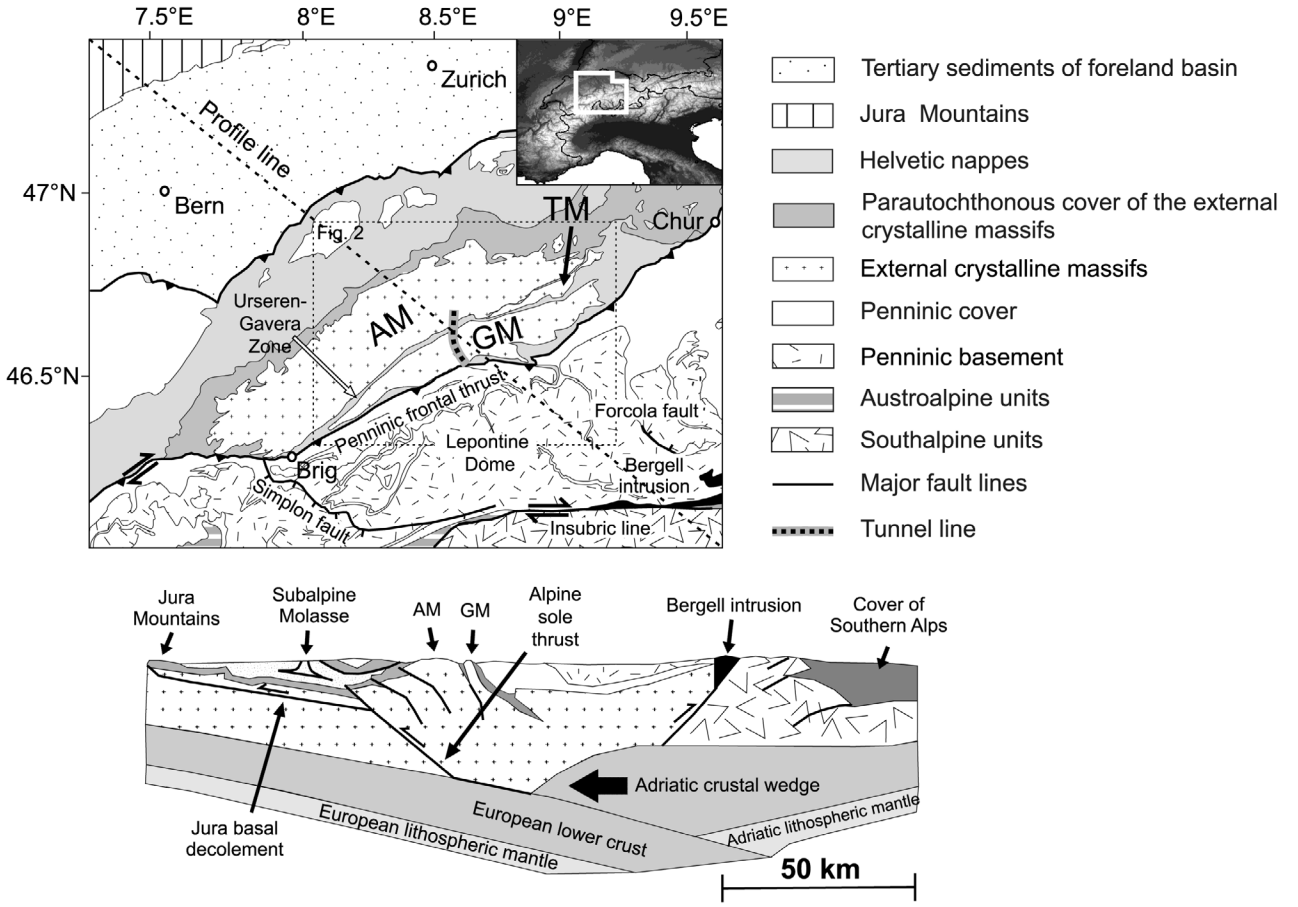

Figure 1. Geological sketch map of central Switzerland [after *Schmid et al.*, 2004] and general crustal cross section along the indicated profile line [after *Schmid et al.*, 1996; *Pfiffner et al.*, 1997b]. Abbreviations are as follows: AM, Aar massif; GM, Gotthard massif; TM, Tavetsch massif.

[10] Apatite fission track (AFT) ages of the GM vary between 4.5 and 14 Ma, similar to AFT ages of the adjacent AM and Penninic nappes [*Hurford*, 1986; *Rahn*, 2005; *Schaer et al.*, 1975; *Steiner*, 1984; *Timar-Geng et al.*, 2004; *Vernon et al.*, 2009; *Wagner and Reimer*, 1972; *Wagner et al.*, 1977]. AFT ages of the GM, with elevations around 2 km, become progressively older from southwest to northeast [*Wagner et al.*, 1977]. No variation in ages is visible across tectonic boundaries, such as the Gavera-Urseren Zone or Penninic frontal thrust [*Hurford*, 1986].

[11] Recently published apatite (U-Th)/He (AHe) ages of the central AM are between 5.2 and 9 Ma [*Vernon et al.*, 2009], similar to corresponding AFT ages. AHe ages range from 2.6 to 7.2 Ma in the Lepontine Dome and are between 2.3 and 6.0 Ma in the southwestern AM [*Dörr*, 2007; *Reinecker et al.*, 2008; *Vernon et al.*, 2009].

[12] Based on the interpretation of age-elevation relationships (AER) and mineral pairs, several authors report exhumation rates of ~0.5 km/Ma during late Miocene times for the central AM and GM [*Hurford*, 1986; *Schaer et al.*, 1975; *Wagner et al.*, 1977]. Quantitative interpretation of thermochronological data (AFT and AHe) in the central AM using 3D numerical thermal modeling with Pecube [*Braun*, 2003], however, shows that the data are best fit by episodic exhumation [*Vernon et al.*, 2009], with two episodes of faster exhumation (from 9 to 7 Ma and 5 to 3 Ma), increasing from 0.3 to 0.7 km/Ma.

4. Principles and Methods

[13] Thermochronology is uniquely suited to reconstruct the cooling and exhumation history of rocks brought to the surface by denudation. Denudation is the removal of rock or soil by tectonic and/or erosional processes at a specific point at the surface [e.g., *Ring et al.*, 1999]. Measured rates of exhumation and denudation are equal only if the particle path of the rock is vertical and the geothermal gradient was constant during the time represented by the thermochronological ages, which is often not the case. For instance, assuming a constant denudation rate, an increase in geothermal gradient will lead to advection of isotherms, and thermochronometers will suggest a decrease in exhumation rate (assuming a constant geothermal gradient for the interpretation). Therefore, exhumation rates derived from thermochronology cannot simply be referred to as denudation rates.

[14] In contrast, surface and rock uplift describe the vertical displacement of Earth's surface and rocks in relation to a

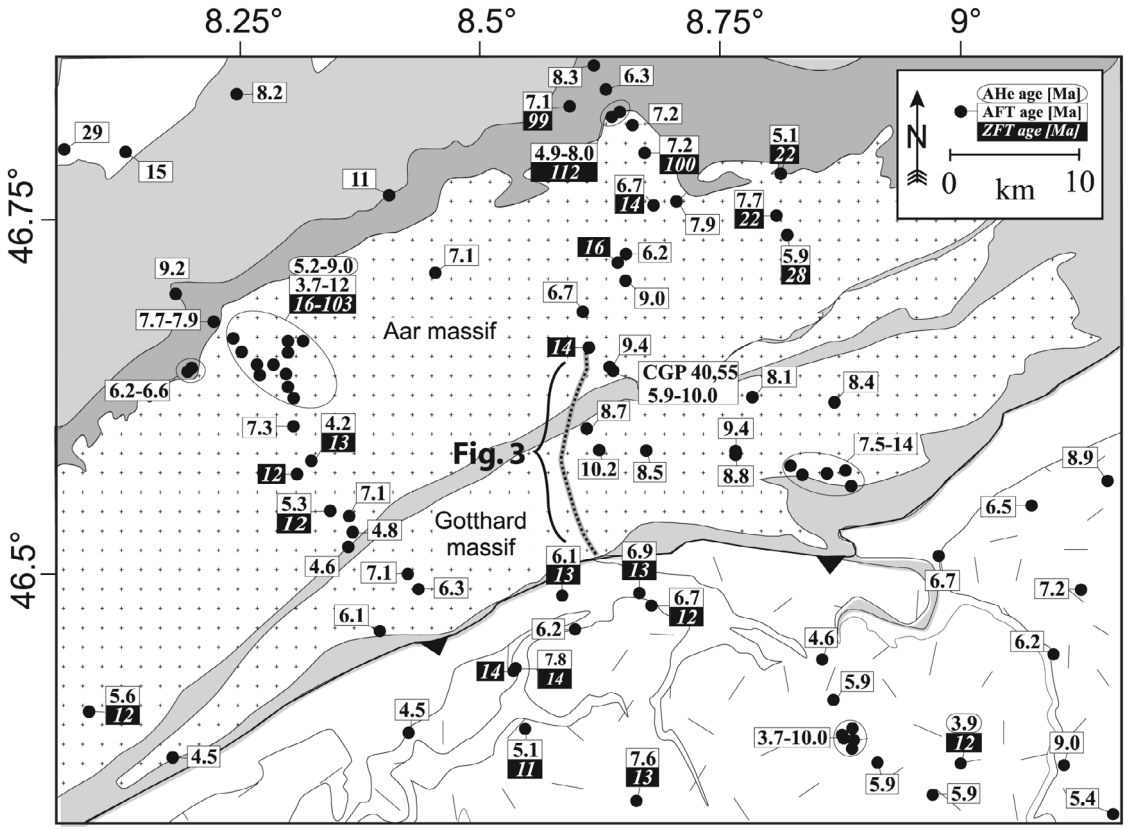

Figure 2. Published ZFT, AFT, and AHe ages in the central AM, GM, and surrounding regions [*Dörr*, 2007; *Hurford*, 1986; *Michalski and Soom*, 1990; *Rahn*, 2005; *Schaer et al.*, 1975; *Soom*, 1989; *Timar-Geng et al.*, 2004; *Wagner et al.*, 1977]. Samples in close vicinity are grouped with ellipses. Thermochronological ages from this study plus previously published ages along the Gotthard transect (dotted line) are reported in Figure 3. Samples from this study which are not located along the transect (CGP 40 and CGP 55a–f) are shown here. Legend as in Figure 1.

defined reference level, e.g., the Earth's geoid [*England and Molnar*, 1990]. Surface and rock uplift are not directly measurable with thermochronology [e.g., *Reiners and Ehlers*, 2005].

4.1. Fission Track Method

[15] The fission track dating method is based on retention of damage trails (fission tracks) continuously produced by spontaneous fission of ^{238}U in U-bearing minerals such as apatite or zircon [*Wagner*, 1968]. Fission tracks shorten (anneal) primarily in response to temperature and time, and thereby act as a form of time recording thermometer [e.g., *Gleadow et al.*, 1986a, 1986b]. The track length distribution can be used for inverse modeling of likely time-temperature (tT) paths [e.g., *Issler et al.*, 1990; *Ketcham et al.*, 1999, 2007a; *Willett*, 1997]. The temperature interval of fission track shortening is called the partial annealing zone (PAZ) [e.g., *Gleadow et al.*, 1986a, 1986b]. For apatite and zircon, the PAZ is usually reported to range approximately from 60°C to 120°C and 190°C to 380°C, respectively [e.g., *Rahn et al.*, 2004; *Wagner and Van den Haute*, 1992]. The temperature of a rock at its thermochronological age is called closure temperature [*Dodson*, 1973]. It ranges from ~80°C and ~190°C for slow cooling rates to ~140°C and 260°C for fast cooling rates for AFT and ZFT, respectively (as calculated by the program Closure [*Brandon et al.*, 1998] for fluorapatite and radiation damaged zircon).

[16] In apatite, fission track annealing kinetics are controlled, besides temperature and time, by the bulk chemical composition (particularly the Cl/F ratio) [e.g., *Green et al.*, 1986]. In general, fluorine rich apatites are less resistant to annealing than chlorine rich apatites [*Gleadow et al.*, 1983, 1986b; *Green et al.*, 1989; *Wagner and Van den Haute*, 1992; *Carlson et al.*, 1999; *Barbarand et al.*, 2003]. Therefore, any meaningful inverse modeling of tT requires determination of the annealing properties of apatites. This can be done either by measuring the chlorine content [*Green et al.*, 1989] or by measuring diameters of etch pits of fission tracks on *c* axis parallel surfaces in apatite grains, so-called Dpar values [*Burtner et al.*, 1994].

[17] The annealing kinetics of zircon fission tracks are, among other factors, a function of radiation damage [*Garver and Kamp*, 2002; *Garver et al.*, 2005; *Rahn et al.*, 2004]. The degree of radiation damage of individual zircon crystals on a microscale can be characterized by Raman spectroscopy [e.g., *Nasdala et al.*, 2001; *Presser and Glotzbach*, 2009].

[18] For detailed information about the FT methodology, the reader is referred to *Galbraith* [2005], *Gallagher et al.* [1998], and *Wagner and Van den Haute* [1992].

4.2. Fission Track Analytical Procedure

[19] Apatite and zircon concentrates were separated using standard magnetic and heavy liquid techniques [e.g., *Danišík*, 2005]. Apatites were mounted in epoxy and zircons in PFA Teflon™, and their surfaces were ground and polished. Apatite mounts were etched with 5M HNO_3 for 20s at 20°C and zircon mounts with a eutectic melt of KOH-NaOH for 27–130 h at 215°C [*Zaun and Wagner*, 1985]. To account for possible variations in etching rates depending on the amount of inserted radiation damage [e.g., *Naeser et al.*, 1987], two mounts with different etching times were prepared for each ZFT sample. Irradiation with thermal neutrons was carried out at the FRM-II reactor facility in Garching (Technical University of Munich, Germany). Mica external detectors were etched to reveal induced tracks using 40% HF at 20°C for 40 min. Fission track counting was carried out with an optical microscope (Zeiss Axioscope 1) under 1000x magnification using a dry objective for AFT analysis and an oil immersion objective for ZFT analysis. Samples were dated by the external detector method [*Gleadow*, 1981; *Naeser*, 1978] using the zeta calibration approach [*Hurford and Green*, 1982, 1983]. Due to low uranium contents and young ages, all apatite samples were irradiated by a collimated beam of heavy ions released from a ^{252}Cf source at the University of Melbourne (Australia) [*Donelick and Miller*, 1991]. This procedure produces additional etching channels, which remarkably enhances the number of etchable confined tracks. Age calculation, visualization and statistics were carried out with the Trackkey 4.2g [*Dunkl*, 2002], and age decomposition with Binomfit [*Brandon*, 1996; *Ehlers et al.*, 2005]. Ages are displayed as central ages and errors as ± 1σ [*Galbraith and Laslett*, 1993]. Where possible, both ZFT mounts per sample were dated and afterward combined into one data value.

[20] Kinetic properties of apatite crystals were determined by measurement of Dpar values (mean of 4 measurements of each apatite crystal), complemented by electron microprobe analysis (University of Tübingen, Germany) using a JEOL Superprobe with a beam current of 30 nA, an acceleration voltage of 15 kV and a beam diameter of 10 μm. Kinetic properties of zircon crystals were estimated by Raman analysis on selected crystals, the results and analytical information are reported by *Presser and Glotzbach* [2009].

4.3. Apatite (U-Th-[Sm])/He Method

[21] (U-Th-[Sm])/He dating is based on the retention and diffusive loss of ^{4}He produced by the decay of ^{238}U, ^{235}U, ^{232}Th and ^{147}Sm [e.g., *Ehlers and Farley*, 2003; *Farley*, 2002; *Lippolt et al.*, 1982; *Reiners and Nicolescu*, 2006; *Zeitler et al.*, 1987]. The resulting AHe age can be calculated from the following equation:

$$^4He = 8 \cdot ^{238}U \cdot \left(e^{\lambda_{238} \cdot t} - 1\right) + 7 \cdot ^{235}U \cdot \left(e^{\lambda_{235} \cdot t} - 1\right) + 6 \cdot ^{232}Th \cdot \left(e^{\lambda_{232} \cdot t} - 1\right) + 1 \cdot ^{147}Sm \cdot \left(e^{\lambda_{147} \cdot t} - 1\right), \quad (1)$$

where ^4He is the radiogenically produced ^{4}He, t is the AHe age, ^{238}U, ^{235}U, ^{232}Th and ^{147}Sm denote the amount of parent isotopes, and λ_{238}, λ_{235}, λ_{232} and λ_{147} are the corresponding decay constants.

[22] Retention and diffusion of ^{4}He is controlled by several factors, including tT history, crystal size and geometry, distribution of parent isotopes and radiation damage of the crystal lattice [e.g., *Shuster et al.*, 2006]. The temperature zone in which ^{4}He is only partially retained is called the partial retention zone (PRZ), which is estimated to be between 40°C and 85°C for apatite [*Wolf et al.*, 1996].

4.4. (U-Th)/He Analytical Procedure

[23] Helium analyses were carried out in the thermochronology laboratory of the University of Tübingen (Germany). Apatite crystals were hand-picked under a stereomicroscope taking into account morphology, size and purity of the crystals. Crystals were inspected at 200x magnification under cross-polarized light for inclusions (all dated crystals were free of visible inclusions). Each selected crystal was digitally photographed parallel and perpendicular to its crystallographic *c* axis and measured. The crystals were loaded into Pt tubes and degassed by laser. U-Th analyses were conducted at the Scottish Universities Environmental Research Centre (SUERC) in East Kilbride (Scotland) and at the University of Melbourne (Australia) using isotope dilution ICP-MS analyses, whereas Sm was only analyzed in samples processed in Melbourne. Further analytical details are given in *Danišík et al.* [2008].

[24] The total analytical uncertainty (TAU) was computed as the square root of the sum of squares of weighted uncertainties on U, Th, (Sm), and He measurements. TAU was between 2 and 9% (1σ) and was used to calculate errors on raw (U-Th)/He ages. Raw (U-Th)/He ages were corrected for the helium loss at the grain margins (alpha ejection correction) [*Farley et al.*, 1996]. An uncertainty of 10% on the alpha ejection correction was assumed and was incorporated in the error calculation of the corrected (U-Th)/He ages.

4.5. Thermal Modeling

[25] The tT paths for individual samples were determined using inverse modeling of AFT and AHe data. Modeling was carried out with the program HeFTy v. 1.6.7 [*Ketcham*, 2005] based on the multikinetic annealing model of *Ketcham et al.* [2007a], with *c* axis projected track length data [*Ketcham et al.*, 2007b] and He diffusion characteristics of Durango apatite [*Farley*, 2000]. The tT paths were statistically evaluated and categorized by a value of goodness of fit (GOF), calculated separately for the age data using equations 31–34 in the work by *Ketcham* [2005] and the AFT length distribution using a Kuiper's test [*Kuiper*, 1960]. A GOF of 0.05 is used as the significance level, below which the null hypotheses, that the modeled length distribution (age) comes from the measured length distribution (age), is rejected. An "acceptable" fit corresponds to a value of 0.05–0.5, a "good" fit corresponds to a value of >0.5, and 1 is the optimum. For details we refer to *Ketcham* [2005].

[26] The input parameters for each sample used in this study were its central FT age with 1σ error, the *c* axis projected track length distribution (if available), the single-grain AHe ages with corresponding sphere radius, U, Th and Sm content and, as a kinetic parameter, the Dpar value. Unless otherwise noted, the initial tT constraints for the modeling were chosen as follows:

[27] 1. The end of the tT path was fixed with the present-day temperature at the sample locality. For the tunnel samples, the temperature measurements reported by *Keller et al.* [1987] were used, and for the surface samples sur-

Table 1. Sample Locations

Sample	Geological Unit	Longitude	Latitude	Elevation (m)
	Surface Samples			
CGP03	Prato Serie	8.58659	46.54844	2250
CGP04	Sorescia Gneiss	8.58189	46.55255	2130
CGP05	Rotondo granite	8.57498	46.56166	2580
CGP06	Guspis Zone	8.57539	46.56544	2520
CGP07	Tremola Series	8.59680	46.53205	1320
CGP08	Gamsboden Granite Gneiss	8.57222	46.57211	2370
CGP09	Gamsboden Granite Gneiss	8.57136	46.57541	2370
CGP10	Gamsboden Granite Gneiss	8.56533	46.58947	1890
CGP11	Gamsboden Granite Gneiss	8.56402	46.59236	1725
CGP12	Gamsboden Granite Gneiss	8.56420	46.60100	1680
CGP13	Gamsboden Granite Gneiss	8.56670	46.60508	1650
CGP14	Northern Paragneiss Zone	8.56789	46.61077	1740
CGP15	Permocarboniferous	8.57292	46.62483	1470
CGP16	Southern Gneiss Zone	8.57584	46.63244	1500
CGP17	Southern Gneiss Zone	8.57922	46.64044	1620
CGP18	Aare Granite	8.58195	46.64480	1800
CGP19	Aare Granite	8.58686	46.65769	1650
CGP20	Aare Granite	8.59232	46.66495	1150
CGP21	Aare Granite	8.58283	46.64700	1650
CGP40	Aare Granite	8.62268	46.65798	2390
CGP41	Aare Granite	8.58442	46.65579	1280
CGP43	Gamsboden Granite Gneiss	8.55921	46.58204	1903
CGP44	Guspis Zone	8.57195	46.56743	2320
CGP45	Fibbia Granite Gneiss	8.56538	46.55768	2091
CGP55a-f	Aare Granite	8.62268	46.65798	2390
MR P 278	Aare Granite	8.59080	46.66101	1265
MR P 291	Gamsboden Granite Gneiss	8.56297	46.59822	1690
MR P 292	Gamsboden Granite Gneiss	8.56912	46.58044	2380
MR P 294	Sorescia Gneiss	8.58149	46.55431	2140
	Tunnel Samples			
MR P 229	Tremola Serie	8.59522	46.53186	1147
MR P 231	Sorescia Gneiss	8.58635	46.54392	1157
MR P 232	Fibbia Granite Gneiss	8.57808	46.55992	1160
MR P 233	Guspis Zone	8.57546	46.56553	1162
MR P 234	Gamsboden Granite Gneiss	8.57247	46.57212	1165
MR P 235	Gamsboden Granite Gneiss	8.57123	46.57511	1166
MR P 236	Gamsboden Granite Gneiss	8.56900	46.58080	1168
MR P 237	Gamsboden Granite Gneiss	8.56553	46.58983	1172
MR P 238	Gamsboden Granite Gneiss	8.56455	46.59281	1173
MR P 239	Gamsboden Granite Gneiss	8.56412	46.59722	1174
MR P 240	Gamsboden Granite Gneiss	8.56552	46.60179	1168
MR P 241	Northern Paragneiss Zone	8.56678	46.60592	1163
MR P 242	Northern Paragneiss Zone	8.56818	46.61058	1157
MR P 244	Permocarboniferous	8.57266	46.62457	1138
MR P 245	Southern Gneiss Zone	8.57557	46.63273	1127
MR P 246	Aare Granite	8.57938	46.64007	1117
MR P 247	Aare Granite	8.58196	46.64481	1110
MR P 248	Aare Granite	8.58522	46.65063	1102
MR P 249	Aare Granite	8.58862	46.65689	1093
MR P 250	Aare Granite	8.59232	46.66495	1082
GSS3800	Sorescia Gneiss	8.58032	46.55885	1158
GSS8220	Gamsboden Granite Gneiss	8.56540	46.59730	1173
GSN4840	Permocarboniferous	8.57593	46.63160	1135

face temperature was calculated assuming a linear correlation of temperature with elevation, with a temperature at sea level of 12.4°C and an atmospheric lapse rate of 4.6°C/km [*Niethammer*, 1910].

[28] 2. We used the corresponding ZFT age and a closure temperature of 230°C–340°C (compare section 4.1) as a "high-temperature" tT constraint. If unavailable, ZFT ages of adjacent samples were used.

5. Results

[29] In total, 34 surface and 23 tunnel samples along the Gotthard transect were dated by at least one thermochronological methods (ZFT, AFT and AHe). Details on sample locations are given in Table 1.

5.1. ZFT Data

[30] ZFT ages were measured on 17 tunnel samples and 20 surface samples, yielding ages between 13.5 and 21.0 Ma (Table 2 and Figure 3). All but one sample (CGP 08) passed the chi-square (χ^2) test at the 5% level, indicating that all samples consisted of single age populations [*Galbraith*, 2005]. Decomposition into different age components yielded two age groups of 12.9 and 19 Ma for sample CGP 08 (Figure 4a).

[31] Raman spectroscopic measurements revealed narrow to moderate bandwidths of 2.34 ± 0.03 to 13.16 ± 0.22 cm^{-1} for the $v_3(SiO_4)$ Raman band at ~1007 cm^{-1} [see *Presser and Glotzbach*, 2009, Table 3]. These values correspond to accumulated radiation doses of $0.08–0.9*10^{18}$ α events/g, using the linear equation from *Nasdala et al.* [2001, equation 5], typical for crystals with very little to little radiation damage [e.g., *Nasdala et al.*, 2001, 2004].

5.2. AFT Data

[32] AFT ages of all tunnel samples and 10 surface samples were previously published by *Glotzbach et al.* [2009]. In addition, in this study AFT ages were measured on 27 surface samples (Table 3 and Figure 3). Dpar values obtained for measured samples were small and relatively uniform, varying between 1.35 and 1.71 μm. Microprobe analyses of 13 samples revealed that all samples were close to F-apatite end-members (Table 4). Furthermore, analyzed elements such as Si, Ce and Sr do not show any significant variation, suggesting that apatites are kinetically uniform.

[33] Tunnel and surface AFT ages range from 5.9 to 12.1 Ma and show a complex relationship with sample elevation throughout the sampled transect. Tunnel samples yielded nearly uniform AFT ages around 6.2 Ma along the tunnel [*Glotzbach et al.*, 2009], whereas surface samples yielded scattered ages (5.9–12.1 Ma). Except sample CGP 03, all samples passed the chi-square (χ^2) test, indicating that these ages represent single populations (Table 3). Identification of single age components for sample CGP 03 suggests two age groups of 7.1 and 11.1 Ma (Figure 4b).

[34] Fission track length data were measured for surface and tunnel samples. Track length distributions were symmetric for long and negatively skewed for short confined MTL, and were between 11.9 and 14.2 μm (Table 5 and Figure 5). MTL and corresponding standard deviations showed a weak correlation with sample elevation, and correlate weakly with AFT age. In the tunnel, MTLs varied

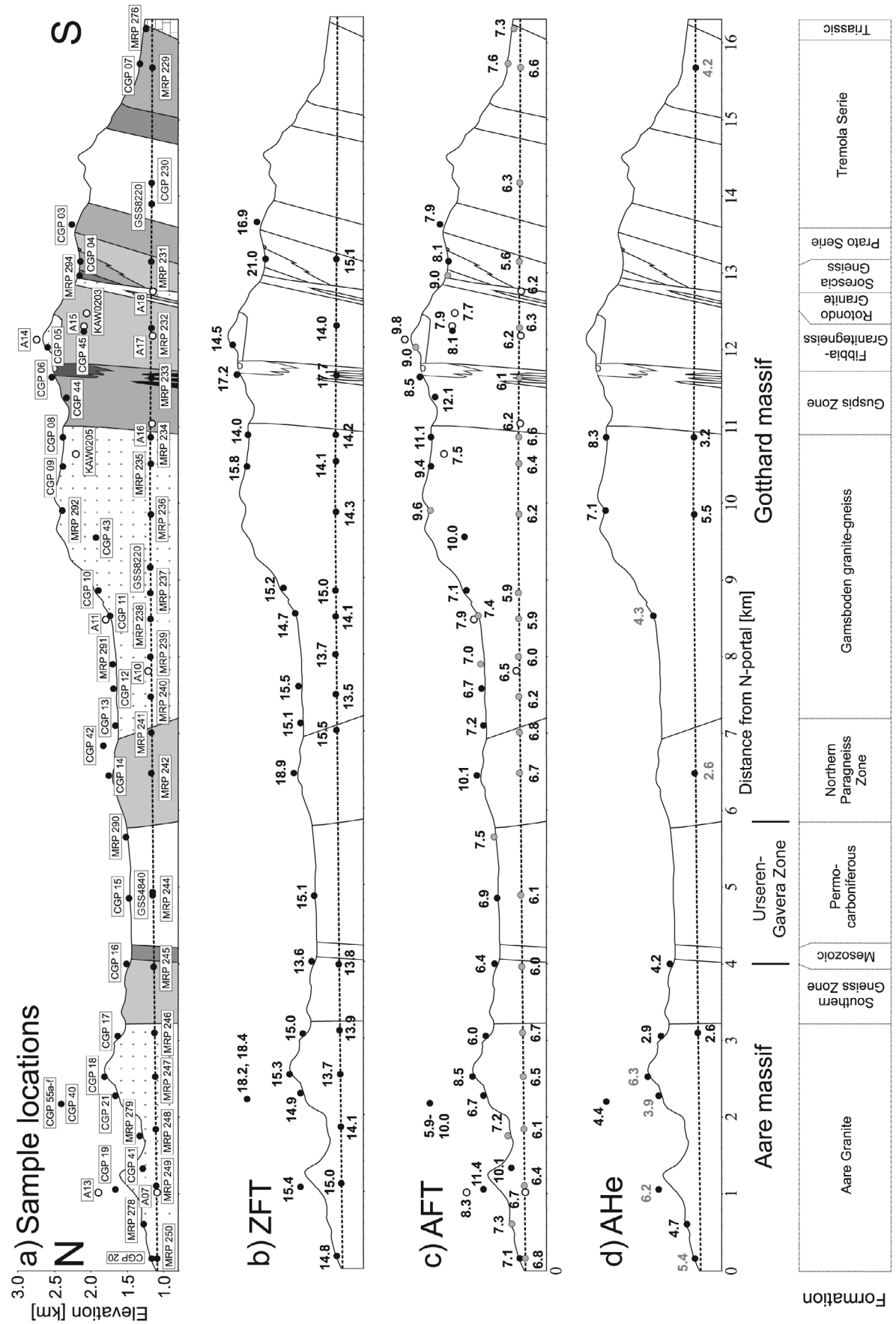
a) Sample locations
N
S
Elevation [km]
b) ZFT
c) AFT
d) AHe
Aare massif
Gotthard massif
Urseren-Gavera Zone
Distance from N-portal [km]
Formation
Aare Granite
Southern Gneiss Zone
Mesozoic
Permo-carboniferous
Northern Paragneiss Zone
Gamsboden granite-gneiss
Gusp is Zone
Fibbia-Granitegneiss
Rotondo Granite
Soresc ia Gneiss
Prato Serie
Tremola Serie
Triassic

Figure 3

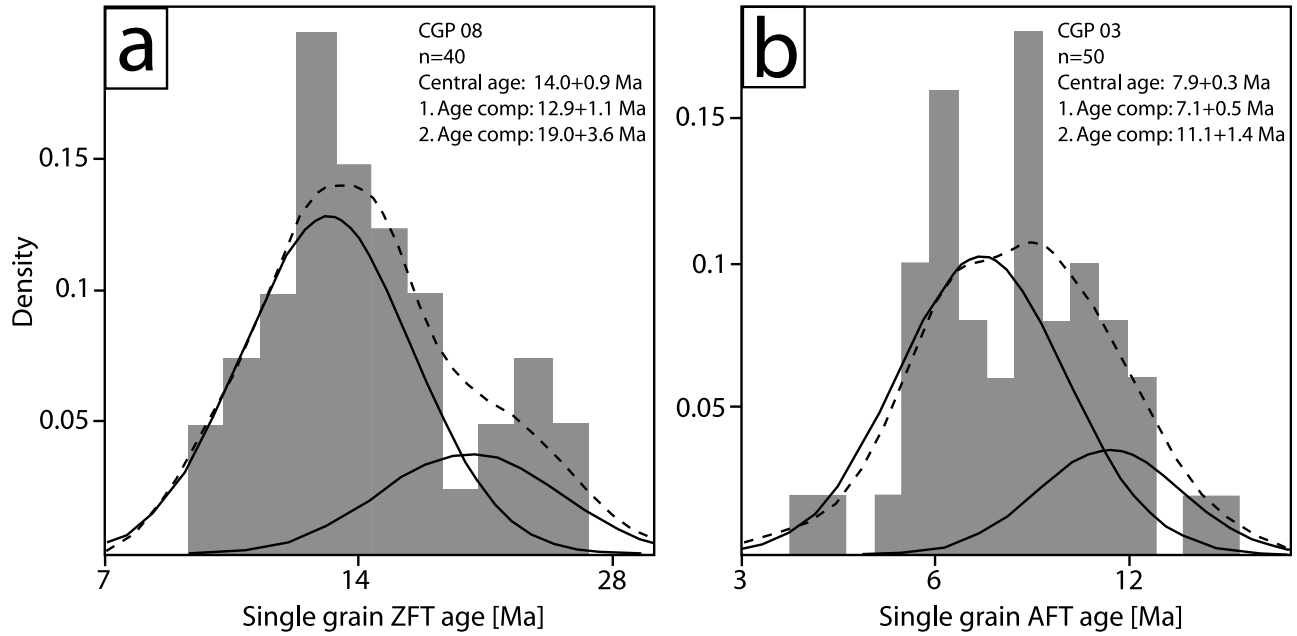

Figure 4. Probability density plots of fission track samples, which did not pass the chi-square test at the 5% level, indicating that they consist of more than one age population. Decomposition into single age components was performed with Binomfit [*Brandon*, 1996; *Ehlers et al.*, 2005], yielding two age groups of (a) ZFT sample CGP 08 and (b) AFT sample CGP 03.

from 11.9 to 13.6 μm. Surface samples yielded MTLs between 12.7 and 14.2 μm, similar to MTLs measured southeast of the GM [*Rahn*, 2005].

5.3. AHe Data

[35] Visual inspection revealed that the majority of samples (42 of 57) did not contain a sufficient amount of datable apatite grains. Therefore, only 49 single apatite crystals from 11 surface and 5 tunnel samples were analyzed by (U-Th)/He and (U-Th-Sm)/He thermochronology, respectively (Table 6). Following the approach proposed by *Fitzgerald et al.* [2006], we used the central AFT age as the criteria to identify outliers of single-grain AHe ages. Ten grains yielded AHe ages older than the corresponding AFT age, and are not incorporated into our interpretation. The fraction of rejected grains (~20%) is comparable to other studies in the Alps [e.g., *Foeken et al.*, 2007; *Glotzbach et al.*, 2008]. We assume that these "too old" ages can be ascribed to He implanted by mineral and fluid inclusions [*Lippolt et al.*, 1994], not visible under 200x magnification and/or phases adjacent to or enclosing the apatite grains (bad neighbors) [*Spiegel et al.*, 2009]. An alternative explanation for these "too old" AHe ages assumes that He retentivity is increased by radiation damage, which increases with U concentrations and time elapsed since the onset of accumulation of radiation damage [e.g., *Green et al.*, 2006; *Shuster et al.*, 2006]. However, for normal U concentration, the effect of radiation damage is most pronounced in slowly cooled terrains, and negligible in regions with young AHe ages, such as the present study area.

[36] Mean AHe ages were calculated for samples with more than one measured crystal, otherwise single-grain AHe ages are reported (Table 6 and Figure 3). In this study we used the degree of replication of single-grain AHe ages as a proxy for the reliability of the resulting mean AHe age. Samples characterized by single-grain AHe age and samples with poorly replicating single-grain ages were not considered in the interpretation, but are shown in Figures 3 and 9 (in gray) for completeness.

[37] Sm was not measured in approximately 40% of analyzed apatites, but corresponding ages were corrected assuming a Sm/eU (eU = effective U, where eU = U + 0.235*Th) ratio of 21.6 ± 14.4 covering the full range of measured ratios (7.2–36.0, Table 6). For instance, grain CGP08#4 yields an (U-Th)/He age of 10 ± 1.1 Ma. Assuming a Sm/eU ratio of 21.6 ± 14.4 the corrected (U-Th-Sm)/He age is 8.6 ± 1.3 Ma. The results suggest that AHe ages would be up to 23% older if the He contribution produced by Sm was neglected, which is similar to results obtained on the Mont Blanc massif [*Glotzbach et al.*, 2008]. Even grains with relatively high U or eU concentrations would be >5% older if the contribution of He from Sm was neglected (Figure 6). In Figure 6b, the Sm contribution to the AHe age is displayed, calculated with equation (1) for a given amount of radiogenic ^{4}He and varying Sm/eU ratios (with fixed eU). Above a Sm/eU ratio

Figure 3. Geological cross section and (a) sample locations, (b) ZFT, (c) AFT, and (d) AHe ages along the Gotthard transect. All ages are given as central ages, and for better readability no errors are given but are reported in Tables 2, 3, and 6. Sample names and locations are from *Glotzbach et al.* [2009] and this study (black dots) and from *Schaer et al.* [1975] and *Wagner et al.* [1977] (open circles). Published AFT ages are from *Glotzbach et al.* [2009] (gray dots) and from *Schaer et al.* [1975] and *Wagner et al.* [1977] (open circles). Single-grain or poorly replicating AHe ages are in gray.

Table 2. ZFT Ages From the Gotthard Transect[a]

Sample	Number of Grains	ρs	Ns	ρi	Ni	ρd	Nd	P(χ^2) (%)	Central ZFT Age ± 1σ (Ma)	U (ppm)
CGP03	40	45.888	1422	61.184	1896	3.055	1480	16	16.9 ± 1.2	620
CGP04	40	45.613	1499	50.299	1653	3.140	1480	97	21.0 ± 1.4	557
CGP05	40	74.921	1708	116.548	2657	3.045	1480	32	14.5 ± 1.0	1193
CGP06	40	72.601	1433	96.464	1904	3.084	1480	98	17.2 ± 1.2	1130
CGP08	40	93.257	1583	150.283	2551	3.053	1480	1	14.0 ± 0.9	1539
CGP09	40	100.668	1222	148.861	1807	3.151	1480	41	15.8 ± 1.1	1469
CGP10	40	70.811	1796	107.281	2721	3.105	1480	25	15.2 ± 1.0	1299
CGP11	20	102.326	717	157.985	1107	3.066	1480	77	14.7 ± 1.1	1586
CGP12	40	85.808	1609	177.270	3324	5.068	3711	99	15.5 ± 0.7	1227
CGP13	40	70.213	1372	106.240	2076	3.099	1480	75	15.1 ± 1.0	1132
CGP14	40	35.597	1342	42.998	1621	3.083	1480	99	18.9 ± 1.3	464
CGP15	20	103.579	1109	156.072	1109	3.070	1480	92	15.1 ± 1.1	1582
CGP16	40	35.370	747	58.855	1243	3.056	1480	25	13.6 ± 1.1	609
CGP17	40	69.857	1303	106.099	1979	3.088	1480	99	15.0 ± 1.0	1040
CGP18	20	77.901	838	117.689	1266	3.132	1480	93	15.3 ± 1.1	1213
CGP19	40	64.624	1435	97.319	2161	3.066	1480	93	15.4 ± 1.0	1076
CGP20	20	64.974	731	101.061	1137	3.107	1480	60	14.8 ± 1.1	1048
CGP21	20	52.944	1045	81.011	1599	3.119	1480	8	14.9 ± 1.1	870
CGP 55a	20	98.077	850	163.153	1414	4.342	1735	56	18.2 ± 1.3	1176
CGP 55f	20	100.406	663	167.949	1109	4.412	1735	73	18.4 ± 1.3	1149
MRP 231	40	47.011	1197	99.796	2541	5.039	3711	100	15.1 ± 0.7	699
MRP 232	40	76.599	1270	174.307	2890	5.055	3711	73	14.0 ± 0.7	1058
MRP 233	40	22.212	1883	28.110	2383	3.027	1480	88	17.7 ± 1.2	314
MRP 234	40	96.299	1264	215.530	2829	5.031	3711	100	14.2 ± 0.7	1351
MRP 235	40	73.756	1696	119.897	2757	3.090	1480	45	14.1 ± 0.9	1350
MRP 236	20	75.126	734	166.423	1626	5.023	3711	60	14.3 ± 0.8	1057
MRP 237	40	107.270	1408	229.320	3010	5.075	3711	98	15.0 ± 0.7	1347
MRP 238	40	70.321	1388	114.652	2263	3.105	1480	74	14.1 ± 1.0	1186
MRP 239	40	82.362	1520	191.384	3532	5.063	3711	65	13.7 ± 0.6	1221
MRP 240	40	79.900	1463	188.491	3460	5.051	3711	96	13.5 ± 0.6	1162
MRP 241	40	64.938	1474	133.488	3030	5.056	3711	93	15.5 ± 0.7	975
MRP 244	20	63.087	716	96.041	1090	3.140	1480	91	15.3 ± 1.2	1089
MRP 245	40	41.858	694	96.261	1596	5.046	3711	100	13.8 ± 0.8	587
MRP 246	40	74.723	1556	169.567	3531	5.022	3711	8	13.9 ± 0.6	1104
MRP 247	44	72.451	1666	167.951	3862	5.036	3711	99	13.7 ± 0.6	1077
MRP 248	41	57.535	1323	129.856	2986	5.048	3711	74	14.1 ± 0.7	1126
MRP 249	40	72.946	1519	156.073	3250	5.053	3711	100	15.0 ± 0.7	974

[a]Abbreviations are as follows: ρs (ρi) are spontaneous (induced) track densities (10^5 tracks/cm^2), Ns (Ni) is number of counted spontaneous (induced) tracks, ρd is dosimeter track density (10^5 tracks/cm^2), Nd is number of tracks counted on dosimeter, P(χ^2) is probability obtaining chi-square value (χ^2) for n degree of freedom (where n is number of crystals minus 1), and ZFT age ± 1σ is central age ± 1 standard error [*Galbraith and Laslett*, 1993]. Ages were calculated using the zeta calibration method [*Hurford and Green*, 1983], glass dosimeter CN-2, and a zeta value of 126 ± 4 yr/cm^2 calculated with Buluk Tuff and Fish Canyon Tuff zircon age standards.

of 6.8 (e.g., 20 ppm U, 20 ppm Th and 168 ppm Sm) the contribution of Sm-produced He to the AHe age exceeds 5%. *Reiners and Nicolescu* [2006] considered several thousand apatite grains with various concentrations of U, Th and Sm (Figure 6a) and concluded that the Sm contribution to the corresponding AHe is <5% for grains with >5 ppm U. It appears that, for the apatite analyzed in this study and in the work of *Glotzbach et al.* [2008], the contribution of He from the Sm parent cannot be ignored if unbiased AHe ages are to be obtained.

[38] Surface samples yielded mean AHe ages between 2.9 to 8.3 Ma. The youngest sample (CGP 17) was located in the SE Aar granite, and oldest ages correspond to the highly elevated samples of the southern transect (CGP 08 and MRP 292). AHe ages along the tunnel were younger than the corresponding ages of the surface samples, and ranged between 2.6 to 5.5 Ma. Again, a sample from the SE Aar granite yielded the youngest age.

6. Interpretation and Discussion

[39] In section 6.1, cooling and exhumation rates are quantified from the thermochronological data set, accompanied by a discussion of the possible impact of near surface processes (fault and hydrothermal activity) on these rates. This is followed by a comparison with exhumation histories predicted for adjacent regions, and interpretation of the resulting geodynamic implications for the evolution of the central Alps.

6.1. Thermal and Exhumation History

[40] Cooling and exhumation rates were derived from (1) combined inverse modeling of AFT and AHe data [e.g., *Ketcham et al.*, 2007a] and (2) the positive correlation of ages with elevation of a single isotopic system [*Schaer et al.*, 1975; *Stüwe et al.*, 1994; *Wagner and Reimer*, 1972].

[41] Most modeled tT paths of tunnel and surface samples are consistent, showing constant to continuously decreasing cooling rates (Figure 7). Some samples in the tunnel (MRP 231, MRP 232, MRP 234) and on the surface (CGP 17, CGP 55e, MRP 291) have stayed longer within the PAZ, followed by slightly faster cooling after ~4 Ma. As the distribution of these slightly aberrant samples does not seem to follow an obvious spatial trend, we relate them to local thermal processes, discussed in section 6.2. For each sample, mean cooling rates for one million year intervals were calculated using the median of

Table 3. Surface AFT Ages of the Gotthard Transect[a]

Sample	Number of Grains	ρs	Ns	ρi	Ni	ρd	Nd	P(χ^2) (%)	Central Age ± 1σ (Ma)	Dpar (μm)	U (ppm)
CGP 03	50	2.115	876	32.873	13616	6.943	3118	0	7.9 ± 0.3	1.47 ± 0.10	58
CGP 04	41	1.664	442	25.019	6647	6.910	3118	100	8.1 ± 0.5	1.63 ± 0.11	48
CGP 06	35	0.447	178	6.407	2552	6.877	3118	100	8.5 ± 0.7	1.38 ± 0.10	10
CGP 08	50	1.738	328	18.988	3583	6.845	3118	100	11.1 ± 0.7	1.50 ± 0.11	33
CGP 09	50	1.392	548	17.243	6788	6.592	3311	29	9.4 ± 0.5	1.44 ± 0.10	30
CGP 10	43	1.469	537	24.194	8844	6.584	3311	39	7.1 ± 0.4	1.47 ± 0.10	41
CGP 12	32	1.672	251	30.252	4541	6.812	3118	97	6.7 ± 0.5	1.42 ± 0.08	50
CGP 13	23	2.232	345	36.196	5594	6.576	3311	21	7.2 ± 0.4	1.54 ± 0.11	67
CGP 14	50	0.750	500	8.624	5752	6.568	3311	65	10.1 ± 0.5	1.55 ± 0.12	16
CGP 15	50	2.145	652	35.951	10928	6.561	3311	99	6.9 ± 0.3	1.49 ± 0.11	77
CGP 16	50	2.955	637	54.009	11641	6.553	3311	34	6.4 ± 0.3	1.71 ± 0.10	100
CGP 17	15	0.474	51	9.185	988	6.545	3311	34	6.0 ± 0.9	1.35 ± 0.13	16
CGP 18	8	0.788	30	11.078	422	6.779	3118	98	8.5 ± 1.6	1.42 ± 0.12	28
CGP 19	23	0.569	79	5.793	805	6.537	3311	6	11.4 ± 1.4	1.44 ± 0.16	12
CGP 20	50	0.527	103	8.543	1671	6.529	3311	67	7.1 ± 0.7	1.48 ± 0.12	15
CGP 21	22	0.526	96	9.031	1648	6.521	3311	76	6.7 ± 0.7	1.38 ± 0.09	19
CGP 40	21	0.702	97	14.096	1949	6.646	3196	18	5.9 ± 0.6	1.37 ± 0.09	24
CGP 41	25	0.614	68	7.162	793	6.660	3196	100	10.1 ± 1.3	1.46 ± 0.08	14
CGP 43	15	3.158	168	37.504	1995	6.689	3196	99	10.0 ± 0.8	1.66 ± 0.14	66
CGP 44	25	0.283	58	2.777	570	6.703	3196	98	12.1 ± 1.7	1.57 ± 0.10	5
CGP 45	25	1.603	214	23.516	3140	6.717	3196	100	8.1 ± 0.6	1.44 ± 0.10	41
CGP 55a	22	0.695	97	14.603	2037	7.788	6103	55	6.5 ± 0.7	1.64 ± 0.14	21
CGP 55b	30	0.859	171	19.655	3913	7.772	6103	100	6.0 ± 0.5	1.54 ± 0.11	31
CGP 55c	30	1.045	157	17.281	2596	7.756	6103	87	8.3 ± 0.7	1.54 ± 0.11	27
CGP 55d	5	1.183	29	19.417	476	7.74	6103	93	8.4 ± 1.6	1.41 ± 0.11	38
CGP 55e	30	1.519	237	25.064	3910	7.788	6103	88	8.4 ± 0.6	1.53 ± 0.11	40
CGP 55f	16	1.099	83	14.949	1129	7.709	6103	100	10.0 ± 1.2	1.45 ± 0.11	24

[a]Abbreviations are as follows: ρs (ρi) is the spontaneous (induced) track density (10^5 tracks/cm^2); Ns (Ni) is the number of counted spontaneous (induced) tracks; ρd is the dosimeter track density (10^5 tracks/cm^2); Nd is the number of tracks counted on the dosimeter; P(χ^2) is the probability of obtaining chi-square value (χ^2) for n degree of freedom (where n is the number of crystals minus 1); and Dpar is the etch pit diameter of fission tracks, averaged from four measurements per analyzed grain with their standard deviation. Ages were calculated using the zeta calibration method [*Hurford and Green*, 1983], glass dosimeter CN-5, and a zeta value of 355 ± 7 yr/cm^2 calculated with Durango and Fish Canyon Tuff apatite standards.

statistically good tT paths, as shown for CGP 20 (Figure 7). Resulting cooling rates are summarized in Figure 8. Rates cluster around the mean of 12°C/Ma, with slightly higher rates between 7 and 10 Ma (17°C–19°C/Ma). Exhumation rates derived from these cooling paths are between 0.4 and 0.8 km/Ma (mean = ~0.5 km/Ma), with highest exhumation rates between 7 and 10 Ma, assuming a constant paleogeothermal gradient of 25°C.

[42] Deriving exhumation rates from age elevation relationships (AER) circumvents any supposition of the geothermal gradient. The resulting exhumation rates, however, are only reliable under several assumptions [e.g., *Parrish*, 1983]: (1) during and after passing through the closure temperature, all samples followed a vertical exhumation pathway and no tectonic displacement existed between sample locations; (2) all samples behave kinetically uniformly; and (3) all samples cooled through the closure temperature at the same elevation with respect to a defined reference horizon, e.g., sea level. These assumptions are all fulfilled for ZFT and AFT ages of the Gotthard transect:

[43] 1. ZFT and AFT ages do not vary along the tunnel, suggesting that vertical offsets have been insignificant since ~14 Ma, and that the samples followed a vertical exhumation pathway.

[44] 2. Dpar and microprobe analyses show that the AFT samples are kinetically uniform. We assume the same to be true for the ZFT samples, as Raman spectroscopy revealed that all measured zircons accumulated only minor radiation damage.

[45] 3. For the given modern relief (~1.5 km), topographic wavelength (~12 km) and an exhumation rate of 0.5 km/Ma, a theoretical topographically induced perturbation of the 100°C isotherm along the Gotthard transect is <200 m [*Stüwe et al.*, 1994], which corresponds to an AFT age perturbation of <0.5 Ma. Further, ZFT and especially AFT ages along the tunnel are consistent within error and show no correlation with superimposed topography (Figure 3). Therefore, we conclude that topography-induced perturbation of isotherms can be neglected for the interpretation of the ZFT and AFT ages along the studied transect. For a more detailed discussion of the influence of topography on the interpretation of thermochronological data along the Gotthard transect, the reader is referred to *Glotzbach et al.* [2009].

[46] The ZFT AER is characterized by a broad positive correlation and three outliers with significantly older ages (Figure 9). Interestingly, these outlier samples have the lowest mean U concentrations of all samples, suggesting a possible correlation between U concentration, corresponding radiation damage, closure temperature and resultant ZFT age. Since Raman data are sparse, U content was used as a proxy for the radiation damage, assuming that accumulation of radiation damage was initiated simultaneously in all samples, a reasonable assumption for samples with the same metamorphic history. Both single-grain and central ZFT ages showed a slight correlation with U content and Raman bandwidths, respectively (Figure 10), suggesting that important differences in the annealing kinetics of ZFT occurs even

Table 4. Composition of Selected Apatite Samples From the Gotthard Transect and From Durango Apatite, With Averages From a Total of 146 Electron Microprobe Analyses[a]

		F		Cl			SiO_2		Ce_2O_3	
Sample	n	Oxide	Ion	Oxide	Ion	OH^- (calc.): Ion	Oxide	Ion	Oxide	Ion
CGP 04	10	3.32 ± 0.14	0.85 ± 0.03	0.03 ± 0.01	0.00 ± 0.00	0.12 ± 0.04	0.10 ± 0.09	0.01 ± 0.01	0.04 ± 0.02	0.00 ± 0.00
CGP 08	10	3.41 ± 0.22	0.89 ± 0.06	0.01 ± 0.01	0.00 ± 0.00	0.09 ± 0.06	0.11 ± 0.05	0.01 ± 0.01	0.11 ± 0.01	0.00 ± 0.00
CGP 09	5	3.61 ± 0.06	0.93 ± 0.02	n.d.	0.00 ± 0.00	0.04 ± 0.02	0.08 ± 0.04	0.01 ± 0.00	0.08 ± 0.02	0.00 ± 0.00
CGP 10	3	3.94 ± 0.07	1.04 ± 0.02	n.d.	0.00 ± 0.00	−0.05 ± 0.02	0.09 ± 0.06	0.01 ± 0.01	0.10 ± 0.02	0.00 ± 0.00
CGP 12	10	4.10 ± 0.23	1.07 ± 0.06	0.01 ± 0.01	0.00 ± 0.00	−0.09 ± 0.07	0.04 ± 0.03	0.00 ± 0.00	0.10 ± 0.02	0.00 ± 0.00
CGP 13	9	3.97 ± 0.09	1.06 ± 0.02	0.01 ± 0.01	0.00 ± 0.00	−0.06 ± 0.02	0.02 ± 0.01	0.00 ± 0.00	0.09 ± 0.02	0.00 ± 0.00
CGP 14	10	3.41 ± 0.16	0.88 ± 0.05	0.01 ± 0.01	0.00 ± 0.00	0.09 ± 0.05	0.04 ± 0.02	0.00 ± 0.00	0.09 ± 0.09	0.00 ± 0.00
CGP 15	9	3.55 ± 0.16	0.91 ± 0.04	n.d.	0.00 ± 0.00	0.06 ± 0.04	0.15 ± 0.15	0.01 ± 0.01	0.13 ± 0.12	0.00 ± 0.00
CGP 16	8	3.18 ± 0.16	0.85 ± 0.04	0.01 ± 0.01	0.00 ± 0.00	0.16 ± 0.04	0.40 ± 0.13	0.03 ± 0.01	0.31 ± 0.06	0.01 ± 0.00
CGP 17	10	4.13 ± 0.17	1.09 ± 0.06	n.d.	0.00 ± 0.00	−0.10 ± 0.05	0.08 ± 0.05	0.01 ± 0.00	0.13 ± 0.04	0.00 ± 0.00
CGP 19	10	3.58 ± 0.16	0.95 ± 0.04	0.01 ± 0.01	0.00 ± 0.00	0.05 ± 0.05	0.14 ± 0.05	0.01 ± 0.00	0.20 ± 0.08	0.01 ± 0.00
CGP 20	10	3.57 ± 0.15	0.94 ± 0.03	0.01 ± 0.01	0.00 ± 0.00	0.05 ± 0.04	0.17 ± 0.15	0.01 ± 0.01	0.23 ± 0.11	0.01 ± 0.00
CGP 21	22	4.02 ± 0.22	1.14 ± 0.06	0.01 ± 0.03	0.00 ± 0.00	−0.11 ± 0.06	0.17 ± 0.14	0.02 ± 0.02	0.20 ± 0.09	0.01 ± 0.00
Durango	20	3.61 ± 0.09	0.95 ± 0.03	0.41 ± 0.02	0.06 ± 0.00	−0.01 ± 0.03	0.48 ± 0.05	0.04 ± 0.00	0.71 ± 0.04	0.02 ± 0.00

	SrO		P_2O_5		CaO				
Sample	Oxide	Ion	Oxide	Ion	Oxide	Ion	Σ	Σ Corrected[b]	Dpar
CGP 04	0.05 ± 0.02	0.00 ± 0.00	44.97 ± 0.47	3.09 ± 0.01	54.57 ± 0.19	4.75 ± 0.03	103.07 ± 0.61	101.67 ± 0.58	1.63 ± 0.11
CGP 08	n.d.	0.00 ± 0.00	44.45 ± 0.46	3.09 ± 0.01	53.82 ± 0.29	4.74 ± 0.02	101.91 ± 0.69	100.47 ± 0.69	1.50 ± 0.11
CGP 09	n.d.	0.00 ± 0.00	44.56 ± 0.17	3.08 ± 0.01	54.59 ± 0.24	4.78 ± 0.02	102.94 ± 0.12	101.41 ± 0.14	1.44 ± 0.10
CGP 10	n.d.	0.00 ± 0.00	43.36 ± 0.41	3.06 ± 0.02	54.26 ± 0.21	4.84 ± 0.04	101.76 ± 0.22	100.10 ± 0.19	1.47 ± 0.10
CGP 12	n.d.	0.00 ± 0.00	44.56 ± 0.40	3.1 ± 0.01	53.71 ± 0.41	4.73 ± 0.03	102.51 ± 0.86	100.78 ± 0.84	1.42 ± 0.08
CGP 13	n.d.	0.00 ± 0.00	43.16 ± 0.70	3.04 ± 0.01	54.42 ± 0.26	4.88 ± 0.03	101.68 ± 0.65	99.80 ± 0.27	1.54 ± 0.11
CGP 14	0.02 ± 0.01	0.00 ± 0.00	45.17 ± 1.34	3.12 ± 0.05	53.71 ± 1.00	4.69 ± 0.13	102.44 ± 0.65	101.00 ± 0.62	1.55 ± 0.12
CGP 15	0.09 ± 0.07	0.00 ± 0.00	44.94 ± 0.36	3.09 ± 0.01	54.59 ± 0.22	4.75 ± 0.02	103.45 ± 0.25	101.96 ± 0.26	1.49 ± 0.11
CGP 16	0.04 ± 0.04	0.00 ± 0.00	41.49 ± 0.35	2.99 ± 0.01	54.41 ± 0.22	4.96 ± 0.02	99.85 ± 0.51	98.51 ± 0.47	1.71 ± 0.10
CGP 17	0.02 ± 0.01	0.00 ± 0.00	42.77 ± 0.24	3.03 ± 0.01	54.61 ± 0.23	4.9 ± 0.02	101.74 ± 0.37	100.00 ± 0.35	1.35 ± 0.13
CGP 19	0.02 ± 0.02	0.00 ± 0.00	42.93 ± 0.50	3.04 ± 0.01	54.54 ± 0.44	4.88 ± 0.02	101.43 ± 0.91	99.92 ± 0.87	1.44 ± 0.16
CGP 20	0.03 ± 0.02	0.00 ± 0.00	43.40 ± 0.56	3.05 ± 0.01	54.43 ± 0.33	4.84 ± 0.03	101.84 ± 0.75	100.33 ± 0.67	1.48 ± 0.12
CGP 21	0.03 ± 0.02	0.00 ± 0.00	42.26 ± 1.40	2.98 ± 0.01	54.33 ± 0.49	5.01 ± 0.03	101.01 ± 1.53	99.79 ± 1.67	1.38 ± 0.09
Durango	0.05 ± 0.02	0.00 ± 0.00	42.78 ± 0.75	3.04 ± 0.02	53.46 ± 0.33	4.8 ± 0.05	101.64 ± 0.81	100.52 ± 0.34	1.63 ± 0.11

[a]Chemical composition is in weight percent and number of atoms per formula unit (apfu); n is the number of measurements, and n.d. means not detected. Detection limits in ppm: F, 140; Cl, 40; SiO_2, 100; Ce_2O_3, 180; SrO, 170; P_2O_5, 470; CaO, 105.

[b]Corrected for OH^- anions.

Table 5. Track Length Data of the Gotthard Transect[a]

Sample	AFT Age ± 1σ (Ma)	# Length	MTL ± SD (μm)	Cor. MTL ± SD (μm)
CGP 04	8.1 ± 0.5	100	14.05 ± 1.20	14.82 ± 0.83
CGP 05	9.0 ± 0.7	57	13.41 ± 1.45	14.56 ± 0.97
CGP 06	8.5 ± 0.7	31	13.71 ± 1.39	14.75 ± 1.05
CGP 07	7.6 ± 0.9	29	13.22 ± 1.55	14.24 ± 1.07
CGP 08	11.1 ± 0.7	100	14.05 ± 1.39	14.85 ± 1.04
CGP 11	7.4 ± 0.4	100	13.15 ± 1.87	14.32 ± 1.35
CGP 14	10.1 ± 0.5	100	13.91 ± 1.37	14.69 ± 1.02
CGP 16	6.4 ± 0.3	100	13.48 ± 1.60	14.44 ± 1.10
CGP 20	7.1 ± 0.7	56	13.28 ± 1.35	14.25 ± 0.96
CGP 55e	8.4 ± 0.6	75	12.87 ± 1.67	13.93 ± 1.36
MRP 231	5.6 ± 0.3	107	11.90 ± 2.00	13.74 ± 1.15
MRP 232	6.3 ± 0.5	86	12.95 ± 1.89	14.30 ± 1.28
MRP 233	6.1 ± 0.4	100	13.56 ± 1.26	14.67 ± 0.89
MRP 235	6.4 ± 0.4	102	13.07 ± 1.70	14.41 ± 1.04
MRP 236	6.2 ± 0.5	66	12.92 ± 1.66	13.92 ± 1.06
MRP 238	5.9 ± 0.4	61	12.88 ± 1.55	14.10 ± 1.29
MRP 240	6.2 ± 0.4	100	13.57 ± 1.61	14.49 ± 1.17
MRP 242	6.7 ± 0.4	100	13.04 ± 1.66	14.12 ± 1.11
MRP 244	6.1 ± 0.3	116	13.55 ± 1.31	14.78 ± 0.81
MRP 245	6.0 ± 0.3	100	13.01 ± 1.87	14.16 ± 1.18
MRP 250	6.8 ± 1.5	94	13.37 ± 2.19	no *c* axis data
MRP 291	7.0 ± 0.4	102	13.08 ± 1.51	14.34 ± 1.02
MRP 292	9.6 ± 0.5	100	14.18 ± 1.72	no *c* axis data
MRP 294	9.0 ± 0.5	100	14.16 ± 1.12	no *c* axis data
GSS3800	no AFT age	36	13.38 ± 1.54	no *c* axis data
GSS8220	no AFT age	100	13.12 ± 1.59	no *c* axis data
GSN4840	no AFT age	100	13.55 ± 1.23	no *c* axis data

[a]Cor. MTL ± SD are *c* axis corrected MTL ± SD, and # length is the number of measured tracks.

at as low a radiation damage level as $0–1*10^{18}$ α fluence/g. Grains and samples with low U concentrations (<600 ppm) and low Raman bandwidths are generally associated with older ages [cf. *Garver et al.*, 2005, Figure 4]. This behavior is exemplified by sample CGP 08, which is characterized by a few old single-grain ages (>20 Ma) and has a low U concentration. As a consequence, this sample failed the chi-square test. Separating the ZFT AER plot into two parts with a threshold U value of 600 ppm removes a great deal of scatter (compare R^2 = 0.41 versus 0.29). Samples with a mean U concentration > 600 ppm yield an apparent exhumation rate of 0.7 km/Ma (0.6–1.0 km/Ma) between 14 and 16 Ma. The given exhumation rates should be viewed with caution, because they were calculated excluding the ZFT data below the threshold value of 600 ppm U. More accurate exhumation rates require field and laboratory studies with greater emphasis on the relationship between accumulated radiation damage and the annealing of ZFT.

[47] Plotting all AFT ages against sample elevation results in a complex AER (Figure 9b). The majority of the data forms a broad positively correlated relationship, with the exception of (1) some high-elevation samples with relatively young ages, which are sampled close to a reactivated fault plane (discussed in section 6.2), and (2) an older group with AFT ages > 10 Ma (Figure 9b, gray ellipse). These old AFT ages are associated with long MTL (~14 μm), and are found in three distinct areas (Figure 3): (1) in the Aar granite (CGP 19 and 41), (2) in the northern Paragneiss zone (CGP 14), and (3) in the southern Gamsboden granite gneiss (CGP 8, 43 and 44). Samples from these regions are distinguished from those from the surrounding areas by clear jumps in ages and track length distributions, both laterally and vertically.

[48] The simplest explanation for these old ages would be that landslide material was inadvertently collected. However, field evidence revealed that these areas are internally intact and that their strike and dip agree with the overall trend. Additionally, corresponding ZFT and AHe data reveal no such jump in ages. Alternative processes explaining the observed age pattern include (1) differences in annealing kinetics, (2) faulting, and/or (3) cold water inflows.

[49] Differences in annealing kinetics can be excluded, because chemical compositions and Dpar values are largely homogenous along the transect. Aberrant AFT ages are restricted to surface samples, whereas corresponding tunnel samples do not deviate from the overall age pattern. Therefore, fault activity and cold water inflows cannot explain these "old ages." Additional field work and detailed sampling are needed to better understand the thermochronological age pattern and their causes, but are beyond the scope of this study.

[50] Nevertheless, after excluding these data, the remaining analyses yield a higher age elevation correlation (compare R^2 = 0.71 versus 0.43) with a slope of 0.5 ± 0.05 km/Ma between 6 and 9 Ma (Figure 9b). Again, the exhumation rate (and particularly the high apparent accuracy) is tenuous since some of the data do not follow this AER.

[51] The AER of the AHe data yields an exhumation rate of 0.2 km/Ma (Figure 9c), but within the 95% confidence interval estimated exhumation rates vary between 0.1 and 1.7 km/Ma. Due to its very low closure temperature, the AHe system is very susceptible to local thermal processes (e.g., hydrothermal activity, frictional heating), which could mask the overall exhumation signal.

[52] Corrected AERs reveal apparently slightly decreasing exhumation rates from around 0.7 km/Ma between 16 and 14 Ma to 0.5 km/Ma between 9 and 6 Ma. In summary, exhumation histories derived from AERs and thermal history modeling are consistent, suggesting nearly uniform exhumation since ~14 Ma at a rate of ~0.5 km/Ma, with only slightly faster exhumation between 16 and 14 Ma and 10 and 7 Ma, at ~0.7 km/Ma.

6.2. Neogene Fault and Hydrothermal Activity Along the Gotthard Transect

[53] The thermochronological data were used to investigate fault activity along the Gotthard transect during the last ~14 Ma. The interpretation is based on the assumption that all samples have the same closure temperature. While this is supported by Dpar and microprobe analyses for the AFT system (Tables 2 and 3), it does not necessarily apply to the ZFT data. The observed variation of ZFT ages along the transect can best be explained by differences in annealing kinetics. With the exception of one sample with the lowest measured mean U concentration (MRP 233), all ZFT ages along the tunnel transect are relatively uniform (14 Ma (Figure 3b)). In addition, AFT ages along the tunnel show no variations in age and, therefore, no fault movement with significant vertical offset has occurred since ~14 Ma.

[54] Based on microthermometric analysis of associated fluid inclusions in quartz, combined with microstructural studies in the Tavetsch massif, *Wyder and Mullis* [1998] suggested a tilting of structures and initiation of brittle deformation between 13 and 17 Ma, and relative uplift of the AM in relation to the GM after 9–11 Ma. In addition,

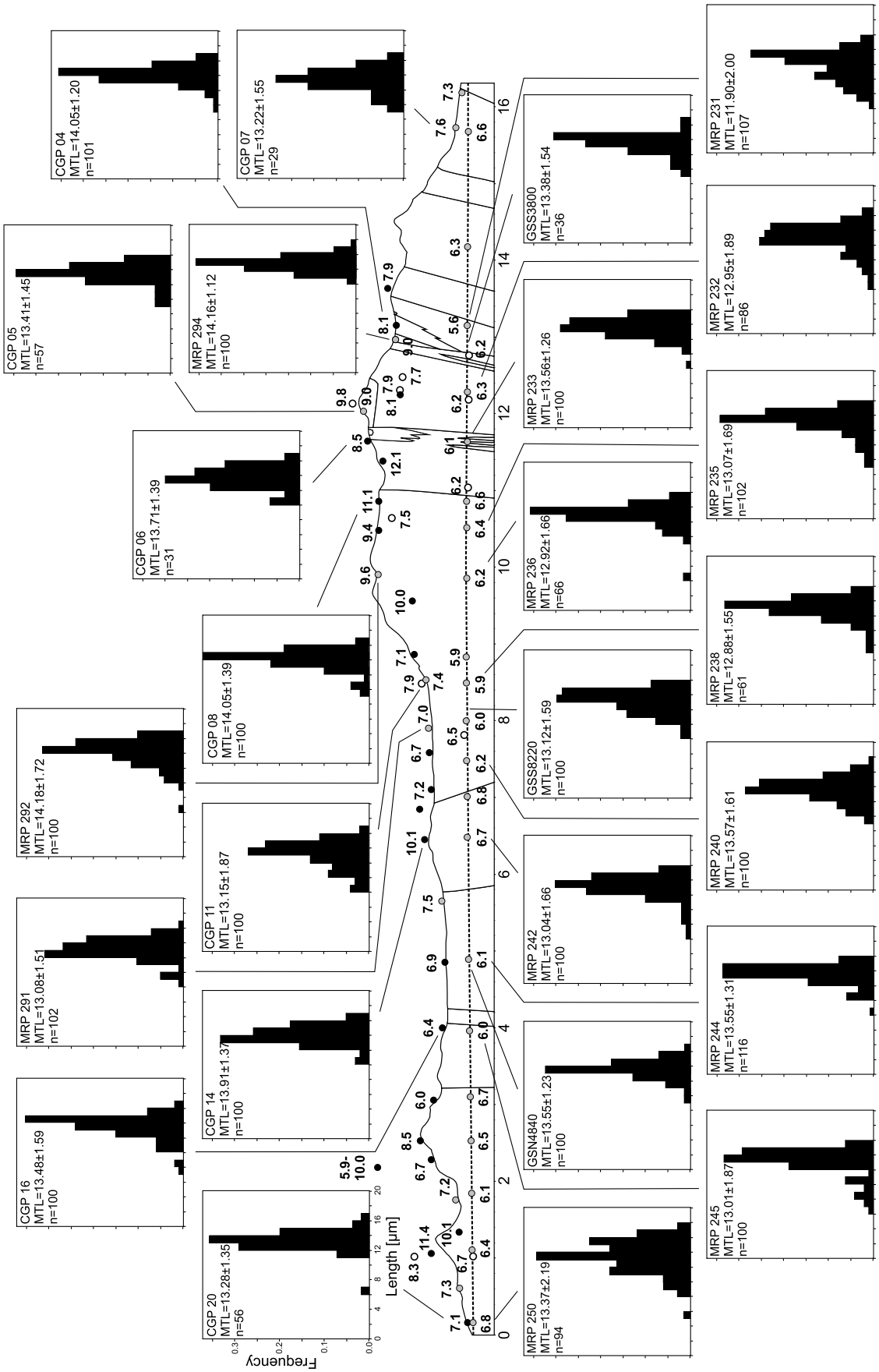

Figure 5. AFT ages and track length distributions along the Gotthard transect. Track length distribution histograms all use the same scale as sample CGP 20. MTL is the mean confined track length with standard deviation uncorrected for track orientation to the crystallographic *c* axis [*Ketcham et al.*, 2007b], and n is the number of measured confined track lengths.

Table 6. AHe Ages of the Gotthard Transect[a]

Sample	AFT Age ± 1σ (Ma)	Th (ng) (Th (ppm))	1σ Error (%)	U (ng) (U (ppm))	1σ Error (%)	Sm (ng) (Sm (ppm))	1σ Error (%)	Th/U	Sm/eU	^{4}He (ncc)	Error (%)	TAU[b] (%)	Raw AHe Age (Ma)	Ft[c]	Corrected AHe Age[d] (Ma)	1σ Error	Excluded Ages[e]	Average AHe Age ± SD[f] (Ma)
CGP 08#2	11.1 ± 0.7	0.0204 (9)	4.4	0.0085 (4)	7.3	n.d.	n.d.	2.4	n.d.	0.014	2.6	8.9	8.7	0.62	12.0 (14.0)	1.9	e	8.3 ± 0.3
CGP 08#4		0.0273 (8)	3.8	0.0475 (14)	4.3	n.d.	n.d.	0.6	n.d.	0.046	0.9	5.8	7.1	0.71	8.6 (10.0)	1.3		
CGP 08#5		0.0244 (16)	4.5	0.0596 (38)	4.1	n.d.	n.d.	0.4	n.d.	0.045	1.2	6.2	5.7	0.62	7.9 (9.2)	1.2		
CGP 11#2	7.4 ± 0.4	0.0517 (21)	3.9	0.0542 (22)	3.8	n.d.	n.d.	1.0	n.d.	0.025	0.9	5.5	3.1	0.62	4.3 (5.0)	0.7		4.3 ± 0.7
CGP 16#3	6.4 ± 0.3	0.3122 (157)	2.3	0.2037 (102)	2.3	n.d.	n.d.	1.5	n.d.	0.112	1	3.4	3.3	0.69	4.2 (4.8)	0.6		4.2 ± 0.2
CGP 16#5		0.4798 (340)	2.2	0.2305 (163)	2.7	n.d.	n.d.	2.1	n.d.	0.118	1	3.6	2.8	0.60	4.1 (4.7)	0.6		
CGP 16#8		0.4398 (303)	1.9	0.1936 (133)	3.0	n.d.	n.d.	2.3	n.d.	0.123	0.9	3.7	3.4	0.65	4.5 (5.2)	0.7		
CGP17#3	6.0 ± 0.9	0.0046 (2)	2.0	0.0124 (5)	2.0	0.2131 (79)	2.0	0.4	15.8	0.033	1.8	2.7	18.9	0.74	25.5 (28.9)	2.6	e	2.9 ± 0.3
CGP17#5		0.0231 (16)	2.0	0.0293 (21)	2.0	0.8719 (619)	2.0	0.8	25.1	0.010	4.5	4.9	2.0	0.60	3.3 (4.0)	0.4		
CGP17#6		0.0406 (24)	2.0	0.0198 (12)	2.0	0.8648 (504)	2.0	2.1	29.5	0.007	6.2	6.5	1.6	0.63	2.6 (3.2)	0.3		
CGP18#8	8.5 ± 1.6	0.0061 (3)	2.0	0.0118 (6)	2.0	0.414 (215)	2.0	0.5	31.4	0.009	5.2	5.6	4.7	0.63	7.4 (9.4)	0.8		6.3 ± 1.5
CGP18#9		0.0139 (8)	2.0	0.017 (10)	2.0	0.444 (265)	2.0	0.8	21.9	0.007	6.2	6.6	2.6	0.64	4.1 (4.9)	0.5		
CGP18#10		0.0367 (21)	2.0	0.0165 (10)	2.0	0.6744 (392)	2.0	2.2	26.8	0.016	3.1	3.7	4.5	0.63	7.2 (8.8)	0.8		
CGP 19#1+4	11.4 ± 1.4	0.0483 (15)	3.7	0.0171 (5)	2.6	n.d.	n.d.	2.8	n.d.	0.018	2.2	5	5.3	0.65	7.0 (8.2)	1.1		6.2 ± 2.4
CGP19#2		0.0263 (16)	2.0	0.0093 (6)	2.0	0.3611 (220)	2.0	2.8	23.4	0.004	3.6	4.1	1.8	0.63	2.9 (3.4)	0.3		
CGP19#3		0.0349 (23)	2.0	0.0144 (10)	2.0	0.3385 (228)	2.0	2.4	15.0	0.013	1.4	2.5	4.2	0.62	6.8 (7.7)	0.7		
CGP19#5		0.0392 (32)	5.0	0.0122 (10)	4.3	n.d.	n.d.	3.2	n.d.	0.017	2.2	7	6.7	0.60	9.6 (11.1)	1.5		
CGP20#7	7.1 ± 0.7	0.0185 (8)	2.0	0.0208 (9)	2.0	0.3816 (157)	2.0	0.9	15.2	0.015	2.6	3.3	4.6	0.66	7.0 (7.9)	0.7		5.4 ± 1.7
CGP20#9		0.0506 (31)	2.0	0.0151 (9)	2.0	0.5209 (317)	2.0	3.4	19.3	0.008	4.7	5.1	2.1	0.62	3.5 (4.0)	0.4		
CGP21#1	6.7 ± 0.7	0.0644 (30)	2.0	0.0267 (12)	2.0	1.2079 (565)	2.0	2.4	28.9	0.016	2.9	3.5	2.6	0.67	3.9 (4.9)	0.4		3.9 ± 0.4
CGP21#4		0.0283 (7)	2.0	0.0146 (4)	2.0	0.5758 (152)	2.0	1.9	27.2	0.079	1.2	2.4	25.9	0.73	35.5 (43.7)	3.6	e	
CGP21#5		0.0037 (1)	2.0	0.0068 (3)	2.0	0.2511 (101)	2.0	0.5	32.6	0.016	3.0	3.6	14.6	0.67	21.8 (28.3)	2.3	e	
CGP55e#1	8.4 ± 0.7	0.0661 (38)	2.0	0.0835 (48)	2.0	0.6942 (398)	2.0	0.8	7.0	0.037	0.9	2.2	3.0	0.64	4.7(4.9)	0.5		4.4 ± 0.2
CGP55e#2		0.0121 (2)	2.0	0.0224 (3)	2.0	0.312 (39)	2.0	0.5	12.4	0.132	0.9	2.2	41.7	0.78	53.7(59.4)	5.5	e	
CGP55e#4		0.1132 (50)	2.0	0.1621 (72)	2.0	1.1434 (507)	2.0	0.7	6.1	0.068	0.9	2.2	2.9	0.65	4.4(4.6)	0.4		
CGP55e#6		0.0653 (29)	2.0	0.0751 (33)	2.0	0.9009 (397)	2.0	0.9	10.0	0.031	1.0	2.2	2.6	0.64	4.1(4.4)	0.4		
CGP55e#7		0.0737 (23)	2.0	0.1085 (34)	2.0	0.8675 (275)	2.0	0.7	6.9	0.051	0.9	2.2	3.2	0.70	4.6(4.9)	0.5		
MRP229#1	6.6 ± 0.7	0.0057 (1)	2.0	0.0103 (1)	2.0	0.0832 (8)	2.0	0.6	7.2	0.005	7.8	8.0	3.4	0.81	4.2 (4.4)	0.5		4.2 ± 0.4
MRP229#3		0.0047 (1)	2.0	0.0039 (1)	2.0	0.1079 (14)	2.0	1.2	21.7	0.006	6.1	6.5	9.9	0.80	12.3 (15.0)	1.2	e	
MRP 234#1	6.6 ± 0.5	0.0195 (13)	6.0	0.0311 (21)	3.9	n.d.	n.d.	0.6	n.d.	0.011	1.1	7.2	2.5	0.63	3.5 (4.0)	0.5		3.2 ± 0.4
MRP 234#3		0.0659 (37)	3.5	0.0755 (42)	2.7	n.d.	n.d.	0.9	n.d.	0.025	3.6	5.7	2.3	0.69	2.9 (3.4)	0.5		
MRP 234#5		0.0525 (2)	3.1	0.0667 (3)	2.3	n.d.	n.d.	0.8	n.d.	0.078	0.9	4.0	8.1	0.69	10.1 (11.8)	1.5	e	
MRP236#2	6.2 ± 0.5	0.0396 (14)	2.0	0.03 (10)	2.0	0.7746 (269)	2.0	1.3	19.7	0.020	2.6	3.3	3.7	0.67	5.6 (6.5)	0.6		5.5 ± 0.4
MRP236#8		0.0552 (25)	2.0	0.0486 (22)	2.0	0.7139 (327)	2.0	1.1	11.6	0.027	2.1	2.9	3.3	0.66	5.0 (5.5)	0.5		
MRP236#10		0.0216 (16)	2.0	0.0356 (26)	2.0	0.4717 (342)	2.0	0.6	11.6	0.019	2.8	3.4	3.5	0.60	5.9 (6.4)	0.6		
MRP236#13		0.0128 (5)	2.0	0.0248 (11)	2.0	0.263 (113)	2.0	0.5	9.5	0.027	2.1	2.9	7.7	0.66	11.6 (12.5)	1.2	e	
MRP 242#2	6.7 ± 0.4	0.0235 (6)	4.3	0.0192 (5)	3.8	n.d.	n.d.	1.2	n.d.	0.007	1.4	5.9	2.2	0.73	2.6 (3.0)	0.4		2.6 ± 0.4
MRP 246#2	6.7 ± 0.5	0.0705 (46)	2.0	0.0314 (21)	2.0	0.9395 (615)	2.0	2.2	19.6	0.007	1.5	3.8	1.09	0.61	1.8 (2.1)	0.2		2.6 ± 0.5
MRP 246#6		0.1464 (43)	2.0	0.0614 (18)	2.0	1.7283 (509)	2.0	2.4	18.0	0.029	1.0	3.6	2.16	0.71	3.0 (3.5)	0.3		
MRP 246#13		0.0591 (31)	2.0	0.0247 (13)	2.0	1.3488 (696)	2.0	2.4	34.9	0.011	1.2	3.7	1.86	0.65	2.9 (3.7)	0.3		
MRP 246#5		0.0537 (16)	2.0	0.0271 (8)	2.0	1.428 (413)	2.0	2.0	36.0	0.011	3.4	4.0	1.8	0.70	2.6 (3.4)	0.3		
MRP 246#14		0.0795 (31)	2.0	0.0424 (17)	2.0	1.3575 (536)	2.0	1.9	22.2	0.015	2.6	3.3	1.7	0.70	2.5 (2.9)	0.3		
MRP 246#17		0.0407 (21)	2.0	0.0265 (13)	2.0	1.1094 (564)	2.0	1.5	30.7	0.005	6.8	7.1	1.0	0.67	1.5 (1.9)	0.2		
MRP 278#4	7.3 ± 0.6	0.0831 (30)	2.7	0.0418 (15)	3.9	n.d.	n.d.	2.0	n.d.	0.025	1.7	5.1	3.3	0.70	4.1 (4.7)	0.6		4.7 ± 0.5
MRP 278#5		0.0543 (22)	3.0	0.0239 (10)	5.4	n.d.	n.d.	2.3	n.d.	0.032	1.4	6.3	7.2	0.67	9.3 (10.8)	1.4	e	
MRP 278#6		0.049 (34)	2.0	0.0116 (8)	2.0	0.624 (438)	2.0	4.2	27.0	0.011	3.5	4.5	3.1	0.61	5.1 (6.2)	0.5		
MRP 292#1	9.6 ± 0.5	0.0429 (12)	3.4	0.0572 (16)	3.4	n.d.	n.d.	0.8	n.d.	0.050	1.2	5.0	6.1	0.72	7.3 (8.5)	1.1		7.1 ± 0.3
MRP 292#2		0.0586 (15)	3.2	0.0882 (23)	3.8	n.d.	n.d.	0.7	n.d.	0.073	1.0	5.1	6.0	0.74	6.9 (8.0)	1.1		
MRP 292#4		0.0202 (11)	4.8	0.0613 (34)	3.2	n.d.	n.d.	0.3	n.d.	0.057	1.1	5.8	7.2	0.64	9.7 (11.2)	1.5	e	

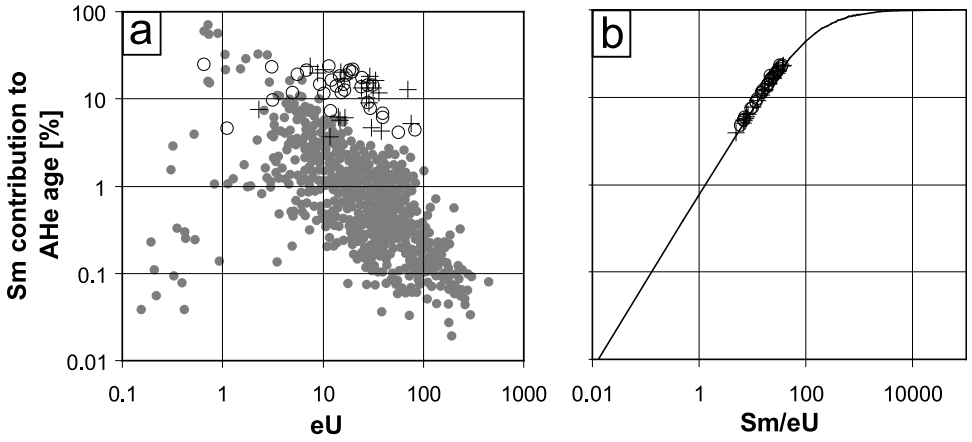

Figure 6. Sm contribution to the (U-Th)/He age (1 − [(U-Th-Sm)/He age/(U-Th)/He age]) in percent plotted against (a) the effective U concentration (eU = U + 0.235*Th) and (b) the Sm/eU ratio. Circles correspond to samples from this study, crosses are from *Glotzbach et al.* [2008], and gray dots are several thousand analyzed samples from the Arizona Radiogenic Helium Dating Laboratory reported by *Reiners and Nicolescu* [2006]. Samples from this study and from *Glotzbach et al.* [2008] have, in general, Sm contributions to the (U-Th-Sm)/He age of >5% even for grains with eU of ≫10. The Sm contribution to the (U-Th)/He age is >5% for Sm/eU ratios of >6.8.

remote sensing analysis, precise leveling and field work demonstrate the existence of a late fracturing phase in the AM and GM [*Dahinden*, 2001; *Persaud and Pfiffner*, 2004; *Zangerl et al.*, 2006]. This event primarily reactivated older faults as a result of postglacial unloading [*Ustaszewski et al.*, 2008]. Postglacial displacements on these faults can exceed 20 m [*Eckhardt et al.*, 1983]. However, our thermochronological data reveal that relative age offsets associated with these deformation phases are small enough to remain within the analytical error of the methods. Regarding the uniform AFT ages along the tunnel (6.2 ± 0.6 Ma) and an exhumation rate of 0.5 km/Ma offsets do not exceed 0.6 km (2 · 0.6 Ma · 0.5 km/Ma). This is in line with structural and mineralogical studies, suggesting that the main phase of brittle deformation had ceased before the structural level of the tunnel samples cooled below 190°C [*Lützenkirchen*, 2002].

[55] The postglacial faults are most abundant in the Urseren valley, where they form uphill-facing scarps with vertical slickensides that follow the distinct subvertical Alpine foliation (Figure 11). Sample CGP 40 was taken from an uphill-facing fault scarp (Figure 11) (fault C4 in the work by *Persaud* [2002]) at an elevation of 2.4 km, which corresponds to the course of the glacial trimline [*Florineth and Schlüchter*, 1998]. It is assumed that the fault scarp is of postglacial age, since it offsets the glacially formed landscape and shows no glacial erosion [*Persaud*, 2002]. Precise leveling across this fault reveals relative vertical movements of 0.5 mm/yr (profile 6 in the work by *Dahinden* [2001]). Surface exposures of the fault comprise mylonitic/augengneiss-like granodiorites, formed by an older ductile deformation event. AFT dating yielded an age of 5.9 Ma, significantly younger than adjacent samples at the same elevation (~9 Ma, compare Figure 3 and 5). Resampling of a 15 m long profile perpendicular to the fault plane showed that this younging in AFT age is restricted to an area within 2 m of the fault plane and that the ZFT system is unaffected (Figure 12).

[56] The AFT age pattern may be explained by localized reheating, either due to (1) frictional heating caused by fault slip events (earthquakes) or (2) hydrothermal activity. Frictional heating generated by a fault slip event produces a very narrow zone (mm- to cm-scale) with very high temperatures (>400°C) [e.g., *Spray*, 1992], and this may reset AFT ages and probably also ZFT ages [*Murakami et al.*, 2006]. However, at shallow depths, shear stress is too low to generate sufficiently large fault slip magnitudes to produce enough frictional heat [*d'Alessio et al.*, 2003], precluding the possibility that postglacial fault slips led to (partial) track annealing.

[57] Relative to frictional heating, hydrothermal activity would lead to a broader (m- to km-scale) thermal anomaly. The samples contain euhedral pyrite, grown on shear surfaces. Since the pyrite was not deformed during development of the schistosity, it was most likely crystallized during

Notes to Table 6:

[a]Th, U, and Sm concentrations in ppm were estimated based on the determined crystal volume and measured contents, assuming an apatite density of 3.2 g/cm^3; n.d., not determined.

[b]The 1σ total analytical error.

[c]Alpha ejection correction factor [*Farley et al.*, 1996].

[d]Single-grain (U-Th)/He (in brackets) and (U-Th-Sm)/He ages are reported, we assumed a Sm/eU ratio of 21.6 ± 14.4 (covering the full range of measured Sm/eU ranging from 7.2 to 36.0) for grains without Sm measurement.

[e]Excluded ages are indicated by e.

[f]Weighted average AHe age with standard deviation is reported for samples with more than one reproducing single-grain AHe ages; otherwise single-grain AHe ages with total analytical error are reported.

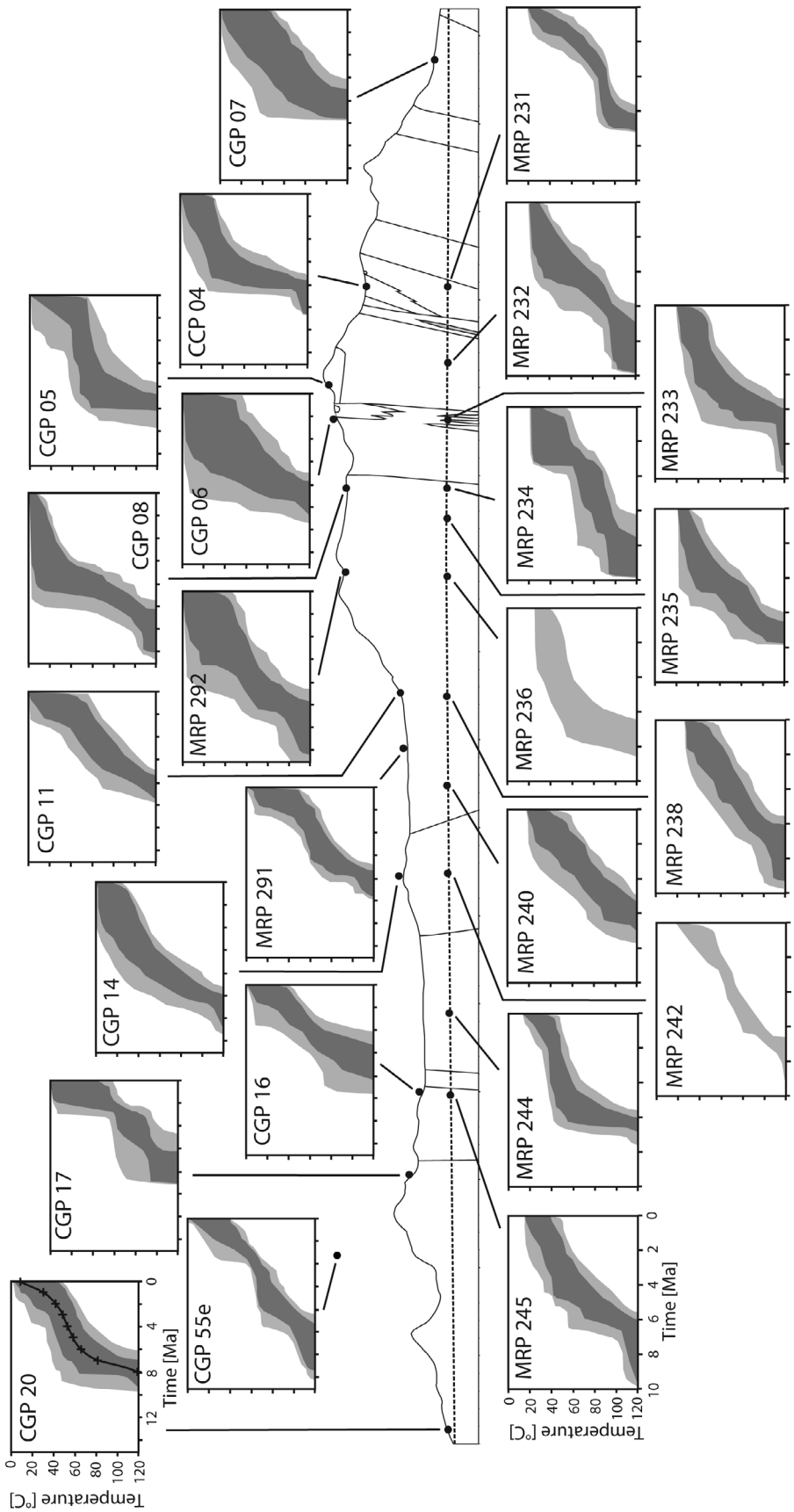

Figure 7. Gotthard transect with results from thermal history modeling. Statistically good (GOF > 0.5) and acceptable (GOF > 0.05) tT paths are shown in dark and light gray, respectively. Modeling results are based on AFT age, AFT track length distributions, and, if available, single-grain AHe ages. Initial tT constraints are the same for all samples: (1) an "upper" constraint is fixed with the present-day outcrop temperature and (2) a "lower" constraint is fixed with corresponding or adjacent ZFT age, assuming a closure temperature of 230°C–340°C calculated with Closure program [*Brandon et al.*, 1998] (compare section 4.1). Axes are shown for one tunnel (MRP 245) and one surface sample (CGP 20) as examples; note the differences in x axes for tunnel and surface samples.

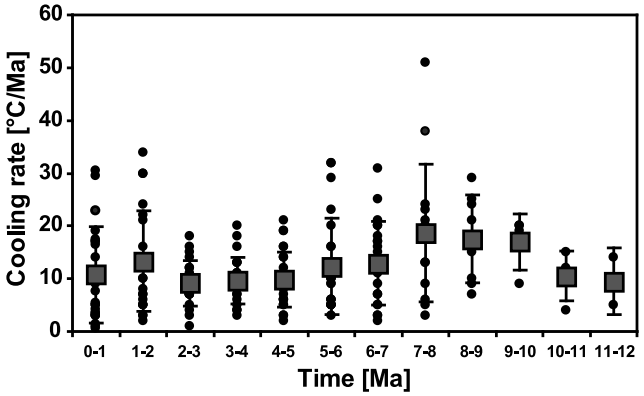

Figure 8. Cooling rates calculated from thermal history modeling of thermochronological data in million year intervals for each sample (black dots) using the median of statistically good tT paths, shown as an example for CGP 20 (Figure 7). Black squares are the means of these median rates with standard deviations.

hydrothermal activity after cessation of deformation. We favor a scenario in which hydrothermal fluids percolated along preexisting and reactivated postglacial fault planes, and partially or fully annealed fission tracks. The timing of fluid activity is difficult to resolve with the data, but is tentatively placed at ~6 Ma, assuming a full resetting of the AFT system. The fluid temperature must be ≫120°C to reset AFT ages close to the fault plane.

[58] Thermal modeling of AFT and AHe data from sample CGP 55e (9 m away from the fault plane) revealed slow cooling and a long stay within the PAZ, followed by increased cooling rates after ~4 Ma (Figure 7). Additional modeling of this sample tested whether the thermochronological data could also be modeled by a reheating event, using two additional tT constraints: (1) assuming that the sample cooled to temperatures between 40°C and 100°C at 8 to 10 Ma in accordance with slightly faster cooling at that time (compare section 6.1) and (2) assuming the sample was further cooled or reheated (depending on the chosen temperature of the previous tT constaint) to temperatures of 40°C to 120°C between 7 and 3 Ma. Resulting statistically good tT paths suggest that the data fit well with reheating up to 110°C, however, the timing is not resolvable.

6.3. Implications for the Geodynamic Evolution of the Central Alps

[59] Exhumation rates derived from thermochronological data are nearly constant since ~14 Ma (~0.5 km/Ma), with

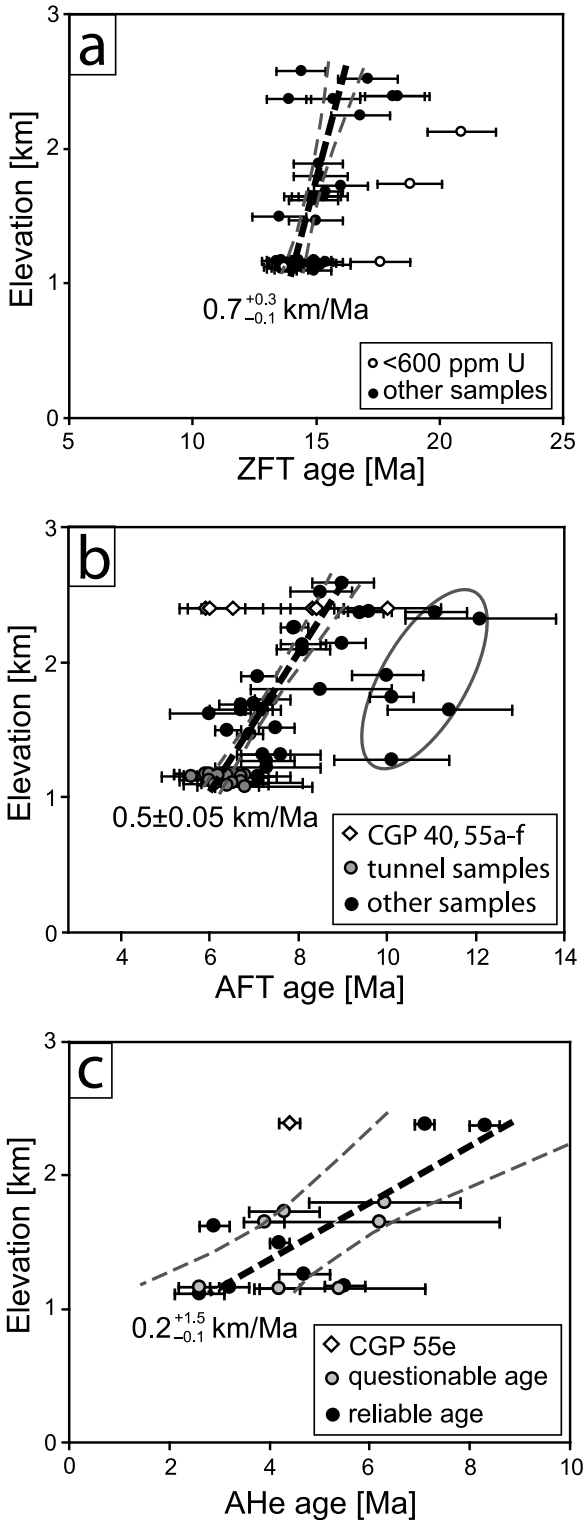

Figure 9. AER of (a) ZFT, (b) AFT, and (c) AHe ages from the Gotthard transect. Good correlations are only obtained after excluding several dates, and therefore, derived exhumation rates are potentially erroneous. Excluding samples with U concentrations of >600 ppm of the ZFT AER yields an exhumation rate of 0.7 km/Ma (min = 0.6, max = 1.0) between 14 and 16 Ma. An exhumation rate of 0.5 ± 0.05 km/Ma between 6 and 9 Ma is obtained excluding fault-affected samples CGP 40 and 55a–f and old ages above 10 Ma (within the ellipse) in the AFT AER. A linear correlation for "reliable" AHe ages suggests an exhumation rate of 0.2 km/Ma (min = 0.1, max = 1.7) between 2 and 8 Ma. Slopes of AER were calculated using least squares fitting of a straight line with elevation as independent variable and central age as dependent variable, weighted according to their errors [e.g., *McCullagh and Nelder*, 1983]. Regression bands were plotted with a 95% confidence interval.

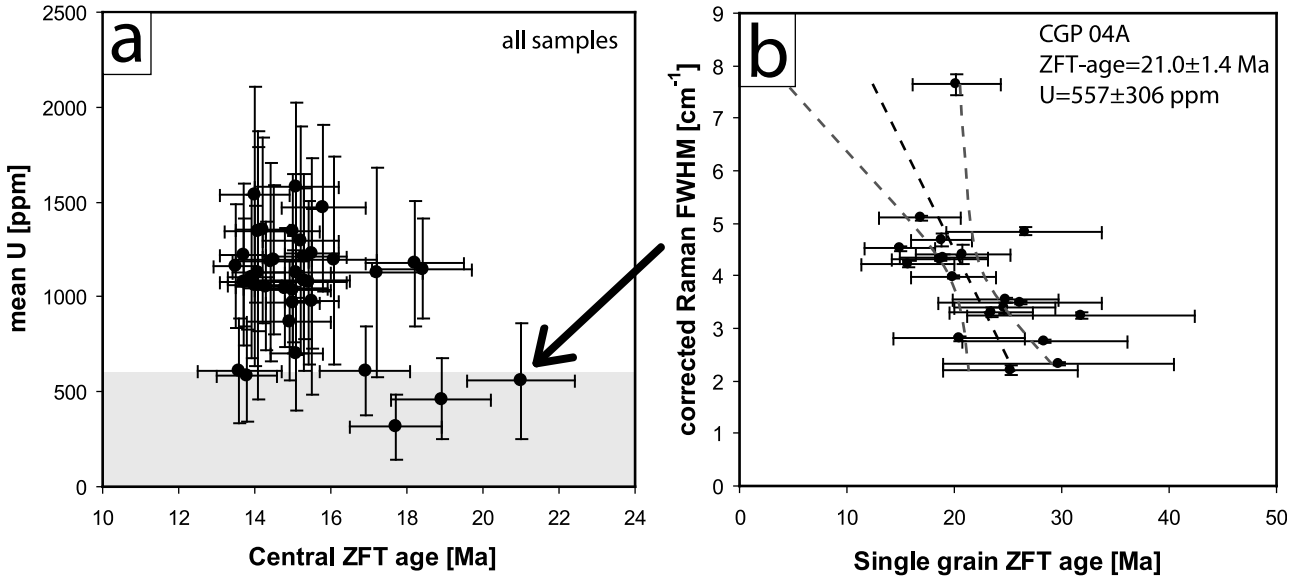

Figure 10. (a) Central ZFT ages plotted against their mean U contents. The gray shaded area refers to mean U concentration of <600 ppm. The arrow points to sample CGP 04A, which was analyzed by Raman spectroscopy [*Presser and Glotzbach*, 2009]. (b) Single-grain ZFT ages plotted against measured Raman bandwidths of the $v_3(SiO_4)$ Raman band at ~1007 cm^{-1} for sample CGP 04A. Linear regression yields a correlation coefficient of 0.28; however, Student's *t* test suggests that it is not significant at a 5% level. The corresponding *t* value is 2.65 and therefore larger than the critical *t* value of 1.73 for 18 degrees of freedom and a significant level of 5%.

slightly faster rates from 16 to 14 Ma (~0.7 km/Ma). The faster exhumation rate probably refers to deep crustal processes: In the Lepontine area SE of the GM, fast cooling started before 20 Ma and subsequently migrated NW, affecting the southeastern part of the GM around 18–15 Ma [*Hurford*, 1986; *Wagner et al.*, 1977]. This migration was likely induced by indentation of the Adriatic crustal wedge, which led to thrusting along the Alpine sole thrust and crustal-scale ramp folding [*Schmid et al.*, 1996, 1997] of the AM and GM, with related updoming and exhumation of the massifs (Figure 1). The fan-shaped (fan structure) arrangement of the main foliation around a NE–SW symmetry plane in the GM [*Zangerl et al.*, 2006], and tilting of structures in the Tavetsch massif at 17–13 Ma [*Wyder and Mullis*, 1998] are most probably associated with this doming and exhumation. At the same time, sediment deposition rates around the Western and Swiss Alps decreased [*Kuhlemann*, 2000], indicating a northward shift of the drainage divide in

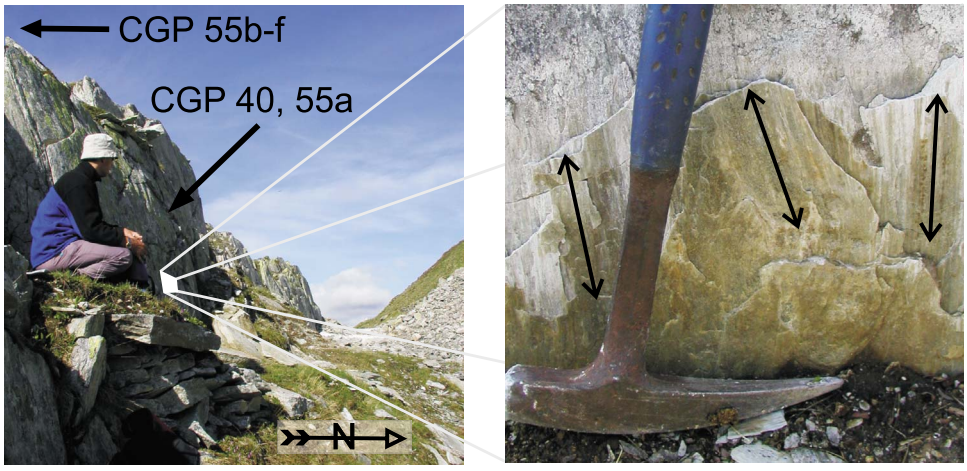

Figure 11. Uphill-facing scarp (profile 6 in the work by *Dahinden* [2001] and fault C4 in the work by *Persaud* [2002]) with an offset of 3 m. Samples CGP 40 and CGP 55a were taken directly from the scarp adjacent to a polished surface (343°/88°) with slickensides, which exhibit nearly vertical orientations. Samples CGP 55b–f were taken perpendicular to the fault scarp in SSE direction.

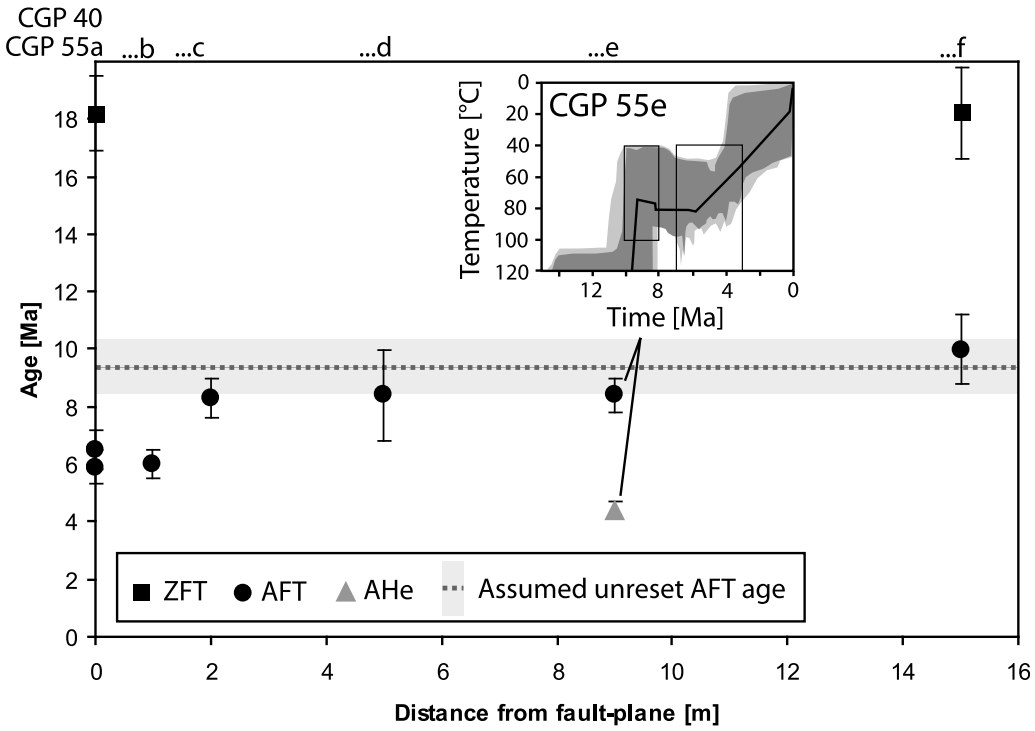

Figure 12. Thermochronological data (AFT, ZFT, and AHe) from samples CGP 40 and 55a–f plotted against the distance to the fault plane shown in Figure 11. For sample CGP 55e tT paths (inset) were modeled using following tT constraints: (1) an "upper" constraint is fixed with the present-day outcrop temperature; (2) a "high-temperature" tT constraint is fixed by the ZFT age of samples CGP 55a and f, assuming a closure temperature of 230°C–340°C calculated with Closure (compare section 4.1) [*Brandon et al.*, 1998]; (3) we assumed that the sample cooled to temperatures between 40°C and 100°C at 8–10 Ma in accordance with fast cooling revealed by adjacent samples (compare section 6.1); and (4) the sample cooled/heated to temperatures of 40°C–120°C between 7 and 3 Ma.

the Alps induced by updoming of the ECMs [*Kuhlemann et al.*, 2001].

[60] The nearly continuous exhumation of the central AM and GM since ~14 Ma at a rate of ~0.5 km/Ma is in accordance with earlier predictions [*Hurford*, 1986; *Schaer et al.*, 1975; *Wagner et al.*, 1977]. Additionally, thermochronological data of the northern Lötschberg transect in the SW AM suggest constant exhumation since ~10 Ma at a rate of ~0.5 km/Ma [*Reinecker et al.*, 2008]. Recently published numerical thermokinematic modeling of thermochronological data, however, suggest a possible episodic exhumation history for the central AM, with faster exhumation from 9 to 7 Ma and 5 to 3 Ma (0.7 km/Ma), and otherwise slower exhumation (0.3 km/Ma) [*Vernon et al.*, 2009]. Interestingly the timing of this first exhumation event coincided with slightly faster exhumation (up to 0.8 km/Ma) predicted by the thermal history modeling of our thermochronological data. However, even our very dense data set gives no unequivocal evidence for the postulated episodic exhumation; thus, its existence remains questionable.

[61] The derived moderate cooling and exhumation since ~16 Ma suggest climate change to wetter conditions at ~5 Ma [*Haug and Tiedemann*, 1998] and related intensification of precipitation in the Alps [*Willett et al.*, 2006] did not markedly affect exhumation in the central AM and GM. In addition, the data suggest that the base level drop due to the Messinian Salinity Crises [*Krijgsman et al.*, 2002] did not lead to enhanced erosion and related acceleration in exhumation in the study area.

[62] The Plio-Pleistocene exhumation history of the study area is different from that of adjacent regions. In contrast to the central AM and GM, the southwestern AM and the area around Chur are characterized by an increase in exhumation rates around 3 Ma [*Reinecker et al.*, 2008; *Vernon et al.*, 2008].

[63] For the area around Chur, *Korup and Schlunegger* [2009] proposed that parts of the "bull's-eye" rock uplift are the consequence of enhanced erosion of mechanically weak outcropping rocks and resulting crustal unloading (Figure 13). However, the coincidence of the high density of historical earthquakes and the abundance of postglacial tectonic activity led *Persaud and Pfiffner* [2004] to suggest that parts of the observed "bull's-eye" rock uplift pattern are caused by active compression at the northeastern rim of the AM. AFT ages for that area are among the youngest within the Alps (<3 Ma), implying that whatever is driving rock uplift (rock-type controlled erosion and related isostatic rebound versus tectonic forcing), it seems that this process is a long-lived feature. Another relatively broad area of rapid rock uplift rates is located southwest of the AM, again

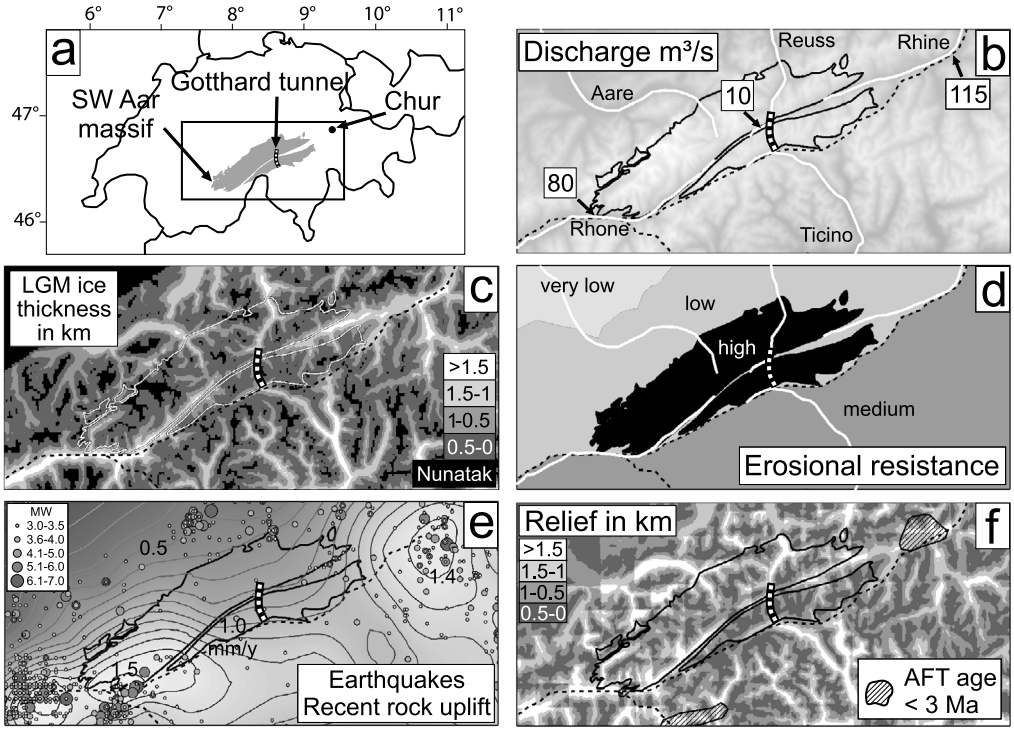

Figure 13. Geomorphological and geological spatial differences in the central Alps: (a) location of study area; (b) discharge [*Schädler and Weingartner*, 1992]; (c) ice thickness of the last glacial maximum (LGM) [*Kelly et al.*, 2004]; (d) erosional resistance estimated from morphometric analyses and geotechnical data [*Kühni and Pfiffner*, 2001; *Schlunegger and Hinderer*, 2001]; (e) recent rock uplift rates [*Kahle et al.*, 1997] and earthquake activity between 1000 and 2007, integrated over different levels of completeness (Earthquake Catalogue of Switzerland, available at http://histserver.ethz.ch); and (f) relief (difference between the maximum elevation in a 10 km radius and the elevation of each pixel) and areas with AFT ages <3 Ma [*Vernon et al.*, 2008].

coinciding with high recent water discharge [*Schädler and Weingartner*, 1992], high LGM ice thicknesses [*Kelly et al.*, 2004] and high density of historical earthquakes (Earthquake Catalogue of Switzerland, available at http://histserver.ethz.ch) (Figure 13). High rock uplift rates may be the result of enhanced erosion and related isostatic rebound. However, compared to the area around Chur, mechanically weak rocks are less abundant (Figure 13). Based on the interpretation of thermochronological data, *Reinecker et al.* [2008] suggested that exhumation was/is primary tectonically controlled. This conclusion is based on the observation that ages decrease close to the Rhône-Simplon fault, and that exhumation rates increased at approximately the same time as extension rotated from orogen-parallel to orogen-perpendicular [e.g., *Sue et al.*, 2007], initiating tectonic denudation in the footwall of the fault.

[64] By contrast, our study area in the central AM and GM has been largely undisturbed by tectonic activity since ~14 Ma, as evidenced by the uniform age pattern along the tunnel transect and by the low density of historical earthquakes (Figure 13). Moreover, we speculate that the area is not likely to have been strongly impacted by a more recent climate change or enhanced glacial/fluvial erosional event. Compared to the area around Chur and the southwest AM, valleys are less deeply incised or broadened, reflected in less distinct relief (Figure 13). Along with low recent discharge rates, the lack of large glaciated valleys and the high erosional resistance of outcropping rocks (Figure 13), it seems that fluvial and glacial erosion is/was less effective. Our data from the central Aar and Gotthard massifs show no evidence for an increase in exhumation rates, but instead it seems that the massifs remained in long-term exhumational steady state since ~14 Ma.

[65] Short-term denudation rates derived from cosmogenic nuclides in river sediments (0.9 ± 0.3 mm/yr averaged for the last 0.4–1.5 ka) [*Wittmann et al.*, 2007] are twice as high as exhumation rates since ~14 Ma (~0.5 km/Ma). This discrepancy can be explained by fluctuations in denudation rates caused by deglaciation, related increased sediment supply and isostatic movements [*Barletta et al.*, 2006; *Champagnac et al.*, 2007, 2009]. Assuming that denudation rates increased sometime after 0.1 Ma (1 Ma) the additional amount of denudation would be <50 m (<500 m) and ages should be <0.1 Ma (<1 Ma) younger, which remains within the analytical error of the presented thermochronological data (e.g., mean error of AFT data is ±0.6 Ma). A much earlier increase in denudation (since 2 or 3 Ma), however, would have led to much younger ages (comparable to that found in the area around Chur and in the southwest AM) and therefore can be ruled out. This suggests a short-term

character to these fluctuations, which may have disturbed the long-term steady state in the recent past.

7. Conclusions

[66] On the basis of thermochronological data (ZFT, AFT and AHe) from the Gotthard transect, several conclusions concerning the thermostructural evolution of the GM and AM can be drawn.

[67] The age pattern along the Gotthard road tunnel is remarkably uniform. Slight variations are more likely due to hydrothermal activity and differences in annealing kinetics rather than to differential exhumation. The observed ZFT age pattern and Raman measurements suggest that even small accumulated radiation damage potentially leads to marked differences in the annealing kinetics of zircon. Excluding these samples, the remaining thermochronological data suggest that vertical offsets along fault structures have been absent since ~14 Ma, except for small movements, e.g., postglacial faulting in the Urseren valley.

[68] Exhumation rates derived from thermal modeling and age-elevation profiles are consistent, suggesting nearly constant exhumation since ~14 Ma at a rate of ~0.5 km/Ma, and only slightly faster exhumation (~0.7 km/Ma) between 16 and 14 Ma, and again between 10 and 7 Ma. The faster exhumation at 16 to 14 Ma is caused by thrusting along the Alpine sole thrust, and updoming and exhumation of the AM and GM related to indentation of the Adriatic wedge. Since ~14 Ma the central AM and GM have been in a long-term exhumational steady state, uninfluenced by climatic change and tectonics.

[69] **Acknowledgments.** Gerlinde Höckh, Dorothea Mühlbayer-Renner, and Dagmar Kost are gratefully acknowledged for mineral separation. Thanks also to Thomas Wenzel for his support during electron microprobe analysis. This study was funded by the German Science Foundation (DFG), project SP673/2-2. We thank Sean Willett, Charlotte Cederbom, and one anonymous reviewer and the associate editor for their constructive comments, which improved the manuscript. English language was improved by Noreen Evans (CSIRO, Exploration and Mining and John de Laeter Centre of Mass Spectrometry, Perth).

References

Barbarand, J., A. Carter, I. Wood, and T. Hurford (2003), Compositional and structural control of fission-track annealing in apatite, *Chem. Geol.*, *198*, 107–137, doi:10.1016/S0009-2541(02)00424-2.

Barletta, V. R., C. Ferrari, G. Diolaiuti, T. Carnielli, R. Sabadini, and C. Smiraglia (2006), Glacier shrinkage and modeled uplift of the Alps, *Geophys. Res. Lett.*, *33*, L14307, doi:10.1029/2006GL026490.

Beaumont, C., P. Fullsack, and J. Hamilton (1992), Erosional control of active compressional orogens, in *Thrust Tectonics*, edited by K. R. McClay, pp. 1–18, Chapman and Hall, New York.

Becker, A. (2000), The Jura Mountains: An active foreland fold-and-thrust belt?, *Tectonophysics*, *321*, 381–406, doi:10.1016/S0040-1951(00)00089-5.

Bogdanoff, S., A. Michard, M. Mansour, and G. Poupeau (2000), Apatite fission track analysis in the Argentera massif: Evidence of contrasting denudation rates in the External Crystalline Massifs of the Western Alps, *Terra Nova*, *12*, 117–125, doi:10.1046/j.1365-3121.2000.00281.x.

Brandon, M. T. (1996), Probability density plot for fission-track grain-age samples, *Radiat. Meas.*, *26*, 663–676, doi:10.1016/S1350-4487(97)82880-6.

Brandon, M. T., M. K. Roden-Tice, and J. I. Garver (1998), Late Cenozoic exhumation of the Cascadia accretionary wedge in the Olympic Mountains, northwest Washington State, *GSA Bull.*, *110*, 985–1009, doi:10.1130/0016-7606(1998)110<0985:LCEOTC>2.3.CO;2.

Braun, J. (2003), Pecube: A new finite-element code to solve the 3D heat equation including the effects of a time-varying, finite amplitude surface topography, *Comput. Geosci.*, *29*, 787–794, doi:10.1016/S0098-3004(03)00052-9.

Burtner, R. L., A. Nigrini, and R. A. Donelick (1994), Thermochronology of Lower Cretaceous source rocks in the Idaho-Wyoming thrust belt, *AAPG Bull.*, *78*, 1613–1636.

Calais, E., J.-M. Nocquet, F. Jouanne, and M. Tardy (2002), Current strain regime in the Western Alps from continuous Global Positioning System measurements, 1996–2001, *Geology*, *30*, 651–654, doi:10.1130/0091-7613(2002)030<0651:CSRITW>2.0.CO;2.

Carlson, W. D., R. A. Donelick, and R. A. Ketcham (1999), Variability of apatite fission-track annealing kinetics: I. Experimental results, *Am. Mineral.*, *84*, 1213–1223.

Cederbom, C. E., H. D. Sinclair, F. Schlunegger, and M. K. Rahn (2004), Climate-induced rebound and exhumation of the European Alps, *Geology*, *32*, 709–712, doi:10.1130/G20491.1.

Champagnac, J. D., P. Molnar, R. S. Anderson, C. Sue, and B. Delacou (2007), Quaternary erosion-induced isostatic rebound in the Western Alps, *Geology*, *35*, 195–198, doi:10.1130/G23053A.1.

Champagnac, J. D., F. Schlunegger, K. Norton, F. von Blanckenburg, L. M. Abbühl, and M. Schwab (2009), Erosion-driven uplift of the modern central Alps, *Tectonophysics*, *474*, 236–249, doi:10.1016/j.tecto.2009.02.024.

Dahinden, T. (2001), Verschiebungsmessungen im Gotthardgebiet, M.S. thesis, ETH Zurich, Zurich, Switzerland.

d'Alessio, M. A., A. E. Blythe, and R. Bürgmann (2003), No frictional heat along the San Gabriel fault, California: Evidence from fission-track thermochronology, *Geology*, *31*, 541–544, doi:10.1130/0091-7613(2003)031<0541:NFHATS>2.0.CO;2.

Danišík, M. (2005), Cooling history and relief evolution of Corsica (France) as constrained by fission track and (U–Th)/He thermochronology, *Tuebinger Geowiss. Arb., Reihe A*, *72*, 1–130.

Danišík, M., R. F. Sachsenhofer, V. A. Privalov, E. A. Panova, W. Frisch, and C. Spiegel (2008), Low-temperature thermal evolution of the Azov Massif (Ukrainian Shield–Ukraine)—Implications for interpreting (U–Th)/He and fission track ages from cratons, *Tectonophysics*, *456*, 171–179, doi:10.1016/j.tecto.2008.04.022.

Dodson, M. H. (1973), Closure temperature in cooling geochronological and petrological systems, *Contrib. Mineral. Petrol.*, *40*, 259–274, doi:10.1007/BF00373790.

Donelick, R. A., and D. S. Miller (1991), Enhanced TINT fission track densities in low spontaneous track density apatites using ^{252}Cf-derived fission fragment tracks: A model and experimental observations, *Nucl. Tracks Radiat. Meas.*, *18*, 301–307, doi:10.1016/1359-0189(91)90022-A.

Dörr, N. (2007), Late-stage exhumation history of the Lepontine dome: Constraints from U-Th/He thermochronology, diploma thesis, Univ. Tübingen, Tübingen, Germany.

Dunkl, I. (2002), Trackkey: A windows program for calculation and graphical presentation of fission track data, *Comput. Geosci.*, *28*(1), 3–12, doi:10.1016/S0098-3004(01)00024-3.

Eckhardt, P., H. Funk, and T. P. Labhart (1983), Postglaziale Krustenbewegungen an der Rhein-Rhone-Linie, *Mensuration Photogramm. Genie Rural*, *2*, 43–56.

Ehlers, T. A., and K. A. Farley (2003), Apatite (U-Th)/He thermochronometry: Methods and applications to problems in tectonic and surface processes, *Earth Planet. Sci. Lett.*, *206*(1–2), 1–14, doi:10.1016/S0012-821X(02)01069-5.

Ehlers, T. A., et al. (2005), Computational tools for low-temperature thermochronometer interpretation, *Rev. Mineral. Geochem.*, *58*, 589–622, doi:10.2138/rmg.2005.58.22.

England, P., and P. Molnar (1990), Surface uplift, uplift of rocks, and exhumation of rocks, *Geology*, *18*, 1173–1177, doi:10.1130/0091-7613(1990)018<1173:SUUORA>2.3.CO;2.

Farley, K. A. (2000), Helium diffusion from apatite I: General behavior as illustrated by Durango fluorapatite, *J. Geophys. Res.*, *105*, 2903–2914, doi:10.1029/1999JB900348.

Farley, K. A. (2002), (U-Th)/He dating; techniques, calibrations, and applications, *Rev. Mineral. Geochem.*, *47*, 819–844, doi:10.2138/rmg.2002.47.18.

Farley, K. A., R. A. Wolf, and L. T. Silver (1996), The effects of long alpha-stopping distances on (U-Th)/He dates, *Geochim. Cosmochim. Acta*, *60*, 4223–4229, doi:10.1016/S0016-7037(96)00193-7.

Fitzgerald, P. G., S. L. Baldwin, L. E. Webb, and P. B. O'Sullivan (2006), Interpretation of (U-Th)/He single grain ages from slowly cooled crustal terranes: A case study from the Transantarctic Mountains of southern Victoria Land, *Chem. Geol.*, *225*, 91–120, doi:10.1016/j.chemgeo.2005.09.001.

Florineth, D., and C. Schlüchter (1998), Reconstructing the Last Glacial Maximum (LGM) ice surface geometry and flowlines in the central Swiss Alps, *Eclogae Geol. Helv.*, *91*, 391–407.

Foeken, J. P. T., C. Persano, F. M. Stuart, and M. ter Voorde (2007), Role of topography in isotherm perturbation: Apatite (U-Th)/He and fission

track results from the Malta tunnel, Tauern Window, Austria, *Tectonics*, *26*, TC3006, doi:10.1029/2006TC002049.
Frey, M., and R. Ferreiro Mählmann (1999), Alpine metamorphism of the central Alps, *Schweiz. Mineral. Petrogr. Mitt.*, *79*(1), 135–154.
Frey, M., E. Jäger, and E. Niggli (1976), Gesteinsmetamorphose im Bereich der Geotraverse Basel-Chiasso, *Schweiz. Mineral. Petrogr. Mitt.*, *56*, 649–659.
Frisch, W. (1979), Tectonic progradation and plate tectonic evolution of the Alps, *Tectonophysics*, *60*, 121–139, doi:10.1016/0040-1951(79)90155-0.
Galbraith, R. F. (2005), *Statistics for Fission Track Analysis*, 219 pp., Chapman and Hall, New York.
Galbraith, R. F., and G. M. Laslett (1993), Statistical models for mixed fission track ages, *Nucl. Tracks Radiat. Meas.*, *21*, 459–470, doi:10.1016/1359-0189(93)90185-C.
Gallagher, K., R. Brown, and C. Johnson (1998), Fission track analysis and its applications to geological problems, *Annu. Rev. Earth Planet. Sci.*, *26*, 519–572, doi:10.1146/annurev.earth.26.1.519.
Garver, J. I., and P. J. J. Kamp (2002), Integration of zircon color and zircon fission-track zonation patterns in orogenic belts: Application to the Southern Alps, New Zealand, *Tectonophysics*, *349*, 203–219, doi:10.1016/S0040-1951(02)00054-9.
Garver, J. I., P. W. Reiners, L. J. Walker, J. M. Ramage, and S. E. Perry (2005), Implications for timing of Andean uplift from thermal resetting of radiation-damaged zircon in the Cordillera Huayhuash, northern Peru, *J. Geol.*, *113*, 117–138, doi:10.1086/427664.
Gleadow, A. J. W. (1981), Fission-track dating methods: What are the real alternatives?, *Nucl. Tracks Radiat. Meas.*, *5*(1–2), 3–14.
Gleadow, A. J. W., I. R. Duddy, and J. F. Lovering (1983), Fission track analysis: A new tool for the evaluation of thermal histories and hydrocarbon potential, *APEA J.*, *23*, 93–102.
Gleadow, A. J. W., I. R. Duddy, and P. F. Green (1986a), Fission track lengths in the apatite annealing zone and the interpretation of mixed ages, *Earth Planet. Sci. Lett.*, *78*, 245–254, doi:10.1016/0012-821X(86)90065-8.
Gleadow, A. J. W., I. R. Duddy, P. F. Green, and J. F. Lovering (1986b), Confined fission track lengths in apatite: A diagnostic tool for thermal history analysis, *Contrib. Mineral. Petrol.*, *94*, 405–415, doi:10.1007/BF00376334.
Glotzbach, C., J. Reinecker, M. Danišík, M. Rahn, W. Frisch, and C. Spiegel (2008), Neogene exhumation history of the Mont Blanc massif, Western Alps, *Tectonics*, *27*, TC4011, doi:10.1029/2008TC002257.
Glotzbach, C., C. Spiegel, J. Reinecker, M. K. Rahn, and W. Frisch (2009), What perturbs isotherms? An assessment using fission track thermochronology and thermal modelling along the Gotthard transect, central Alps, in *Thermochronological methods: From Paleotemperature Constraints to Landscape Evolution Models*, edited by F. Lisker et al., *Geol. Soc. Spec. Publ.*, *324*, 111–124.
Green, P. F., I. R. Duddy, A. J. W. Gleadow, P. R. Tingate, and G. M. Laslett (1986), Thermal annealing of fission tracks in apatite: 1. A qualitative description, *Chem. Geol.*, *59*, 237–253, doi:10.1016/0009-2541(86)90048-3.
Green, P. F., I. R. Duddy, G. M. Laslett, K. A. Hegarty, A. J. W. Gleadow, and J. F. Lovering (1989), Thermal annealing of fission tracks in apatite: 4. Quantitative modeling techniques and extension to geological timescales, *Chem. Geol.*, *79*, 155–182.
Green, P. F., P. V. Crowhurst, I. R. Duddy, P. Japsen, and S. P. Holford (2006), Conflicting (U-Th)/He and fission track ages in apatite: Enhanced He retention, nor anomalous annealing behaviour, *Earth Planet. Sci. Lett.*, *250*, 407–427, doi:10.1016/j.epsl.2006.08.022.
Gubler, E. (1976), Beitrag des Landesnivellements zur Bestimmung vertikaler Krustenbewegung in der Gotthard-Region, *Schweiz. Mineral. Petrogr. Mitt.*, *56*, 675–678.
Haug, G. H., and R. Tiedemann (1998), Effect of the formation of the Isthmus of Panama on Atlantic Ocean thermohaline circulation, *Nature*, *393*, 673–676, doi:10.1038/31447.
Hurford, A. J. (1986), Cooling and uplift patterns in the Lepontine Alps south central Switzerland and an age of vertical movement on the Insubric fault line, *Contrib. Mineral. Petrol.*, *92*, 413–427, doi:10.1007/BF00374424.
Hurford, A. J., and P. F. Green (1982), A users' guide to fission track dating calibration, *Earth Planet. Sci. Lett.*, *59*, 343–354, doi:10.1016/0012-821X(82)90136-4.
Hurford, A. J., and P. F. Green (1983), The Zeta age calibration of fission-track dating, *Chem. Geol.*, *41*, 285–317, doi:10.1016/S0009-2541(83)80026-6.
Issler, D. R., C. Beaumont, S. D. Willett, R. A. Donelick, J. Mooers, and A. Grist (1990), Preliminary evidence from apatite fission track data concerning the thermal history of the Peace River Arch Region, Western Canada Sedimentary Basin, *Bull. Can. Pet. Geol.*, *38A*, 250–269.
Kahle, H.-G., et al. (1997), Recent crustal movements, geoid and density distribution; contribution from integrated satellite and terrestrial measurements, in *Results of NRP 20: Deep Structure of the Swiss Alps*, edited by O. A. Pfiffner et al., pp. 251–259, Birkhaeuser, Basel, Switzerland.
Keller, F., H. Wanner, and T. R. Schneider (1987), *Geologischer Schlussbericht Gotthard-Strassentunnel*, *Beitr. zur Geol. der Schweiz: Geotechn. Ser.*, vol. 70, Kümmerly and Frey, Bern.
Kelly, M. A., J.-F. Buoncristiani, and C. Schlüchter (2004), A reconstruction of the last glacial maximum (LGM) ice-surface geometry in the western Swiss Alps and contiguous Alpine regions in Italy and France, *Eclogae Geol. Helv.*, *97*, 57–75, doi:10.1007/s00015-004-1109-6.
Ketcham, R. A. (2005), Forward and inverse modelling of low-temperature thermochronology data, *Rev. Mineral. Geochem.*, *58*, 275–314, doi:10.2138/rmg.2005.58.11.
Ketcham, R. A., R. A. Donelick, and W. D. Carlson (1999), Variability of apatite fission-track annealing kinetics: III. Extrapolation to geologic time scales, *Am. Mineral.*, *84*, 1235–1255.
Ketcham, R. A., A. Carter, R. A. Donelick, J. Barbarand, and A. J. Hurford (2007a), Improved modeling of fission-track annealing in apatite, *Am. Mineral.*, *92*, 799–810, doi:10.2138/am.2007.2281.
Ketcham, R. A., A. Carter, R. A. Donelick, J. Barbarand, and A. J. Hurford (2007b), Improved measurement of fission-track annealing in apatite using *c* axis projection, *Am. Mineral.*, *92*, 789–798, doi:10.2138/am.2007.2280.
Kirschner, L., M. A. Cosca, H. Masson, and J. C. Hunziker (1996), Staircase $^{40}Ar/^{39}Ar$ spectra of fine-grained white mica: Timing and duration of deformation and empirical constraints on argon diffusion, *Geology*, *24*, 747–750, doi:10.1130/0091-7613(1996)024<0747:SAASOF>2.3.CO;2.
Korup, O., and F. Schlunegger (2009), Rock-type control on erosion-induced uplift, eastern Swiss Alps, *Earth Planet. Sci. Lett.*, *278*, 278–285, doi:10.1016/j.epsl.2008.12.012.
Krijgsman, W., M.-M. Blanc-Valleron, R. Flecker, F. J. Hilgen, T. J. Kouwenhoven, D. Merle, F. Orszag-Sperber, and J.-M. Rouchy (2002), The onset of the Messinian salinity crisis in the eastern Mediterranean (Pissouri Basin, Cyprus), *Earth Planet. Sci. Lett.*, *194*, 299–310, doi:10.1016/S0012-821X(01)00574-X.
Kuhlemann, J. (2000), Post-collisional sediment budget of circum-Alpine basins (central Europe), *Mem. Ist. Geol. Mineral. Univ. Padova*, *52*, 1–91.
Kuhlemann, J. (2007), Paleogeographic and paleotopographic evolution of the Swiss and Eastern Alps since the Oligocene, *Global Planet. Change*, *58*, 224–236, doi:10.1016/j.gloplacha.2007.03.007.
Kuhlemann, J., W. Frisch, I. Dunkl, B. Székely, and C. Spiegel (2001), Miocene shifts of the drainage divide in the Alps and their foreland basin, *Z. Geomorphol.*, *45*, 239–265.
Kühni, A., and O. A. Pfiffner (2001), The relief of the Swiss Alps and adjacent areas and its relation to lithology and structure: Topographic analysis from a 250-m DEM, *Geomorphology*, *41*, 285–307, doi:10.1016/S0169-555X(01)00060-5.
Kuiper, N. H. (1960), Tests concerning random points on a circle, *Proc. K. Ned. Akad. Wet., Ser. A Math. Sci.*, *63*, 38–47.
Labhart, T. P. (1977), *Aarmassiv und Gotthardmassiv*, 173 pp., Gebr. Borntraeger, Berlin.
Lippolt, H. J., W. Boschmann Käthler, and H. Arndt (1982), Helium und Uran in Schwarzälder Bleiglanzen, ein Datierungsversuch, *Oberrheinische Geol. Abh.*, *31*, 31–46.
Lippolt, H. J., M. Leitz, R. S. Wernicke, and B. Hagedorn (1994), (Uranium+thorium)/helium dating of apatite: Experience with samples from different geochemical environments, *Chem. Geol.*, *112*, 179–191, doi:10.1016/0009-2541(94)90113-9.
Lützenkirchen, V. H. (2002), Structural geology and hydrogeology of brittle fault zones in the central eastern Gotthard massif, Switzerland, Ph.D. thesis, ETH Zurich, Zurich, Switzerland.
McCullagh, P., and J. A. Nelder (1983), *Generalized Linear Models*, Chapman and Hall, London.
Michalski, I., and M. Soom (1990), The Alpine thermo-tectonic evolution of the Aar and Gotthard massifs, central Switzerland: Fission track ages on zircon and apatite and K-Ar mica ages, *Schweiz. Mineral. Petrogr. Mitt.*, *70*, 373–387.
Murakami, M., R. Yamada, and T. Tagami (2006), Short-term annealing characteristics of spontaneous fission tracks in zircon: A qualitative description, *Chem. Geol.*, *227*, 214–222, doi:10.1016/j.chemgeo.2005.10.002.
Naeser, C. W. (1978), Fission track dating, *U.S. Geol. Surv. Open File Rep.*, *76-190*.
Naeser, N. D., P. K. Zeitler, C. W. Naeser, and P. F. Cerveny (1987), Provenance studies by fission track dating of zircon-etching and counting procedures, *Nucl. Tracks Radiat. Meas.*, *13*, 121–126, doi:10.1016/1359-0189(87)90022-7.

Nasdala, L., M. Wenzel, G. Vavra, G. Irmer, T. Wenzel, and B. Kober (2001), Meamictisation of natural zircon: Accumulation versus thermal annealing of radioactivity-induced damage, *Contrib. Mineral. Petrol.*, *141*, 125–144.

Nasdala, L., P. W. Reiners, J. I. Garver, A. K. Kennedy, R. A. Stern, E. Balan, and R. Wirth (2004), Incomplete retention of radiation damage in zircon from Sri Lanka, *Am. Mineral.*, *89*, 219–231.

Niethammer, G. (1910), Die Wärmeverteilung im Simplon, *Eclogae Geol. Helv.*, *11*, 96–120.

Nocquet, J.-M., and E. Calais (2004), Geodetic measurements of crustal deformation in the western Mediterranean and Europe, *Pure Appl. Geophys.*, *161*, 661–681, doi:10.1007/s00024-003-2468-z.

Parrish, R. R. (1983), Cenozoic thermal evolution and tectonics of the Coast Mountains of British Columbia, 1. Fission track dating, apparent uplift rates, and patterns of uplift, *Tectonics*, *2*(6), 601–631, doi:10.1029/TC002i006p00601.

Persaud, M. (2002), Active tectonics in the eastern Swiss Alps, Ph.D. thesis, 115 pp., Univ. Bern, Bern.

Persaud, M., and O. A. Pfiffner (2004), Active deformation in the eastern Swiss Alps: Post-glacial faults, seismicity and surface uplift, *Tectonophysics*, *385*, 59–84, doi:10.1016/j.tecto.2004.04.020.

Pfiffner, O. A., S. Sahli, and M. Stäuble (1997a), Compression and uplift of the external massifs in the Helvetic zone, in *Deep Structure of the Swiss Alps: Results of NRP 20*, edited by O. A. Pfiffner et al., pp. 139–153, Birkhäuser, Boston, Mass.

Pfiffner, O. A., P.-F. Erard, and M. Stäuble (1997b), Two cross sections through the Swiss Molasse Basin (lines E4–E6, W1, W7–W10), in *Deep Structure of the Swiss Alps: Results of NRP 20*, edited by O. A. Pfiffner et al., pp. 64–72, Birkhäuser, Boston, Mass.

Presser, V., and C. Glotzbach (2009), Metamictization in zircon: Raman investigation following a Riefveld approach. Part II: Sampling depth implication and experimental data, *J. Raman Spectrosc.*, *40*(5), 499–508, doi:10.1002/jrs.2154.

Rahn, M. K. (2005), Apatite fission track ages from the Adula nappe: Late-stage exhumation and relief evolution, *Schweiz. Mineral. Petrogr. Mitt.*, *85*, 233–245.

Rahn, M. K., M. T. Brandon, G. E. Batt, and J. I. Garver (2004), A zero-damage model for fission-track annealing in zircon, *Am. Mineral.*, *89*, 473–484.

Reinecker, J., M. Danišík, C. Schmid, C. Glotzbach, M. Rahn, W. Frisch, and C. Spiegel (2008), Tectonic control on the late stage exhumation of the Aar Massif (Switzerland): Constraints from apatite fission track and (U-Th)/He data, *Tectonics*, *27*, TC6009, doi:10.1029/2007TC002247.

Reiners, P. W., and T. A. Ehlers (2005), *Low-Temperature Thermochronology: Techniques, Interpretations, and Applications*, *Rev. in Mineral. and Geochem.*, vol. 58, 622 pp., Mineral. Soc. of Am., Washington, D. C.

Reiners, P. W., and S. Nicolescu (2006), Measurement of parent nuclides for (U-Th)/He chronometry by solution sector ICP-MS, *ARHDL Rep.*, *1*, Ariz. Radiogenic Helium Dating Lab., Tucson. (Available at http://www.geo.arizona.edu/~reiners/arhdl/arhdl_reports.htm)

Ring, U., M. T. Brandon, S. Willett, and G. S. Lister (1999), Exhumation processes, in *Exhumation Processes: Normal Faulting, Ductile Flow and Erosion*, edited by U. Ring et al., *Geol. Soc. Spec. Publ.*, *154*, 1–28.

Rolland, Y., M. Rossi, S. F. Cox, M. Corsini, N. Mancktelow, G. Pennacchioni, M. Fornari, and A. M. Boullier (2008), $^{40}Ar/^{39}Ar$ dating of synkinematic white mica: Insights from fluid-rock reaction in low-grade shear zones (Mont Blanc Massif) and constraints on timing of deformation in the NW external Alps, in *The Internal Structure of Fault Zones: Implications for Mechanical and Fluid-Flow Properties*, edited by C. A. J. Wibberley et al., *Geol. Soc. Spec. Publ.*, *299*, 293–315.

Schädler, B., and R. Weingartner (1992), Natural runoff 1961–1980, in *Hydrological Atlas of Switzerland*, edited by R. Weingartner and M. Spreafico, panel 5.4, Swiss Fed. Off. for Water and Geol., Bern.

Schaer, J. P., G. M. Reimer, and G. A. Wagner (1975), Actual and ancient uplift rate in the Gotthard region, Swiss Alps: A comparison between precise levelling and Fission-Track Apatite age, *Tectonophysics*, *29*, 293–300, doi:10.1016/0040-1951(75)90154-7.

Schaltegger, U. (1994), Unravelling the pre-Mesozoic history of Aar and Gotthard massifs (central Alps) by isotopic dating—A review, *Schweiz. Mineral. Petrogr. Mitt.*, *74*, 41–51.

Schlunegger, F., and M. Hinderer (2001), Crustal uplift in the Alps: Why the drainage pattern matters, *Terra Nova*, *13*, 425–432, doi:10.1046/j.1365-3121.2001.00374.x.

Schlunegger, F., D. Rieke-Zapp, and K. Ramseyer (2007), Possible environmental effects on the evolution of the Alps-Molasse Basin system, *Swiss J. Geosci.*, *100*, 383–405, doi:10.1007/s00015-007-1238-9.

Schmid, S. M., O. A. Pfiffner, N. Froitzheim, G. Schönborn, and E. Kissling (1996), Geophysical-geological transect and tectonic evolution of the Swiss-Italian Alps, *Tectonics*, *15*, 1036–1064, doi:10.1029/96TC00433.

Schmid, S. M., O. A. Pfiffner, G. Schönborn, N. Froitzheim, and E. Kissling (1997), Integrated cross section and tectonic evolution of the Alps along the Eastern Traverse, in *Deep Structure of the Swiss Alps: Results of NRP 20*, edited by O. A. Pfiffner et al., pp. 289–304, Birkhäuser, Boston, Mass.

Schmid, S. M., B. Fuegenschuh, E. Kissling, and R. Schuster (2004), Tectonic map and overall architecture of the Alpine orogen, *Eclogae Geol. Helv.*, *97*, 93–117, doi:10.1007/s00015-004-1113-x.

Shuster, D. L., R. M. Flowers, and K. A. Farley (2006), The influence of natural radiation damage on helium diffusion kinetics in apatite, *Earth Planet. Sci. Lett.*, *249*, 148–161, doi:10.1016/j.epsl.2006.07.028.

Soom, M. (1989), Spaltspurendatierungen entlang des NFP 20-Westprofils (Externmassive und Penninikum), *Schweiz. Mineral. Petrogr. Mitt.*, *69*, 191–192.

Spiegel, C., B. Kohn, D. Belton, Z. Berner, and A. Gleadow (2009), Apatite (U-Th-Sm)/He thermochronology of rapidly cooled samples: The effect of He implantation, *Earth Planet. Sci. Lett.*, *285*, 105–114, doi:10.1016/j.epsl.2009.05.045.

Spray, J. G. (1992), A physical basis for the frictional melting of some rock-forming minerals, *Tectonophysics*, *204*, 205–221, doi:10.1016/0040-1951(92)90308-S.

Steck, A., and J. Hunziker (1994), The Tertiary structural and thermal evolution of the central Alps—Compressional and extensional structures in an orogenic belt, *Tectonophysics*, *238*, 229–254, doi:10.1016/0040-1951(94)90058-2.

Steiner, H. (1984), Radiometrische Altersbestimmungen an Gesteinen der Maggia-Decke (Penninikum der Zentralalpen), *Schweiz. Mineral. Petrogr. Mitt.*, *64*, 227–259.

Stüwe, K., L. White, and R. Brown (1994), The influence of eroding topography on steady-state isotherms. Application to fission track analysis, *Earth Planet. Sci. Lett.*, *124*, 63–74, doi:10.1016/0012-821X(94)00068-9.

Sue, C., B. Delacou, J.-D. Champagnac, C. Allanic, P. Tricart, and M. Burkhard (2007), Extensional neotectonics around the bend of the western/central Alps: An overview, *Int. J. Earth Sci.*, *96*, 1101–1129, doi:10.1007/s00531-007-0181-3.

Timar-Geng, Z., D. Grujic, and M. K. Rahn (2004), Deformation at the Leventina-Simano nappe boundary, central Alps, Switzerland, *Eclogae Geol. Helv.*, *97*, 265–278, doi:10.1007/s00015-004-1121-4.

Ustaszewski, M., A. Hampel, and O. A. Pfiffner (2008), Composite faults in the Swiss Alps formed by the interplay of tectonics, gravitation and postglacial rebound: An integrated field and modelling study, *Swiss J. Geosci.*, *101*, 223–235, doi:10.1007/s00015-008-1249-1.

Vernon, A., P. van der Beek, H. Sinclair, and M. K. Rahn (2008), Increase in late Neogene denudation of the European Alps confirmed by isoage analysis of a fission-track database, *Earth Planet. Sci. Lett.*, *270*, 316–329, doi:10.1016/j.epsl.2008.03.053.

Vernon, A., P. van der Beek, H. Sinclair, C. Persano, J. Foeken, and F. M. Stuart (2009), Variable late Neogene exhumation of the central European Alps: Low-temperature thermochronology from the Aar Massif, Switzerland, and the Lepontine Dome, Italy, *Tectonics*, *28*, TC5004, doi:10.1029/2008TC002387.

von Raumer, J. F., and F. Neubauer (1993), *Pre-Mesozoic Geology in the Alps*, Springer, Berlin.

Wagner, G. A. (1968), Fission track dating of apatites, *Earth Planet. Sci. Lett.*, *4*, 411–415, doi:10.1016/0012-821X(68)90072-1.

Wagner, G. A., and G. M. Reimer (1972), Fission track tectonics: The tectonic interpretation of fission track apatite ages, *Earth Planet. Sci. Lett.*, *14*, 263–268, doi:10.1016/0012-821X(72)90018-0.

Wagner, G. A., and P. Van den Haute (1992), *Fission-Track Dating*, 285 pp., Kluwer Acad., Dordrecht, Netherlands.

Wagner, G. A., G. M. Reimer, and E. Jäger (1977), Cooling ages derived by apatite fission track, mica Rb-Sr and K-Ar dating: The uplift and cooling history of the central Alps, *Mem. Ist. Geol. Mineral. Univ. Padova*, *30*, 1–27.

Whipple, K. X. (2009), The influence of climate on the tectonic evolution of mountain belts, *Nat. Geosci.*, *2*, 97–104, doi:10.1038/ngeo413.

Whipple, K. X., and B. J. Meade (2006), Orogen response to changes in climatic and tectonic forcing, *Earth Planet. Sci. Lett.*, *243*, 218–228, doi:10.1016/j.epsl.2005.12.022.

Willett, S. D. (1997), Inverse modeling of annealing of fission tracks in Apatite 1: A controlled random search method, *Am. J. Sci.*, *297*, 939–969.

Willett, S. D., C. Beaumont, and P. Fullsack (1993), Mechanical model for the tectonics of doubly vergent compressional orogens, *Geology*, *21*, 371–374, doi:10.1130/0091-7613(1993)021<0371:MMFTTO>2.3.CO;2.

Willett, S. D., F. Schlunegger, and F. Picotti (2006), Messinian climate change and erosional destruction of the central European Alps, *Geology*, *34*, 613–616, doi:10.1130/G22280.1.

Wittmann, H., F. von Blanckenburg, T. Kruesmann, K. P. Norton, and P. W. Kubik (2007), Relation between rock uplift and denudation from cosmo-

genic nuclides in river sediment in the central Alps of Switzerland, *J. Geophys. Res.*, *112*, F04010, doi:10.1029/2006JF000729.

Wolf, R. A., K. A. Farley, and L. T. Silver (1996), Helium diffusion and low-temperature thermochronometry of apatite, *Geochim. Cosmochim. Acta*, *60*, 4231–4240, doi:10.1016/S0016-7037(96)00192-5.

Wyder, R. F., and J. Mullis (1998), Fluid impregnation and development of fault breccias in the Tavetsch basement rocks (Sedrun, central Swiss Alps), *Tectonophysics*, *294*, 89–107, doi:10.1016/S0040-1951(98)00130-9.

Zangerl, C., S. Loew, and E. Eberhardt (2006), Structure, geometry and formation of brittle discontinuities in anisotropic crystalline rocks of the Central Gotthard Massif, Switzerland, *Eclogae Geol. Helv.*, *99*, 271–290, doi:10.1007/s00015-006-1190-0.

Zaun, P. E., and G. A. Wagner (1985), Fission-track stability in zircons under geological conditions, *Nucl. Tracks Radiat. Meas.*, *10*, 303–307, doi:10.1016/0735-245X(85)90119-X.

Zeitler, P. K., A. L. Herczig, I. McDougall, and M. Honda (1987), U-Th-He dating in apatite: A potential thermochronometer, *Geochim. Cosmochim. Acta*, *51*, 2865–2868, doi:10.1016/0016-7037(87)90164-5.

M. Danišík, John de Laeter Centre of Mass Spectrometry, Applied Geology, Curtin University of Technology, Perth, WA 6845, Australia. (m.danisik@curtin.edu.au)

W. Frisch and J. Reinecker, Institute for Geoscience, University of Tübingen, Sigwartstr. 10, D-72076 Tübingen, Germany. (frisch@uni-tuebingen.de; john.reinecker@uni-tuebingen.de)

C. Glotzbach, Institute of Geology, University of Hannover, Calinstr. 30, D-30167 Hannover, Germany. (glotzbach@geowi.uni-hannover.de)

M. Rahn, Institute of Geoscience, University of Freiburg, Albertstr. 23-B, D-79104 Freiburg, Germany. (meinert.rahn@hsk.ch)

C. Spiegel, FB 5: Geoscience, University of Bremen, Klagenfurter Straße, D-28359 Bremen, Germany. (cornelia.spiegel@uni-bremen.de)